membranes

MDPI

Article

The Recycle Effect on Permeate Flux in Double-Pass Flat-Plate Air-Gap Membrane Distillation (AGMD) Modules

Chii-Dong Ho [1,*], Jyun-Jhe Li [1], Jun Wei Lim [2] and Yu-Chih Zhang [1]

[1] Department of Chemical and Materials Engineering, Tamkang University, Tamsui, New Taipei 251301, Taiwan; 613400398@o365.tku.edu.tw (J.-J.L.); 614400082@o365.tku.edu.tw (Y.-C.Z.)
[2] HICoE-Centre for Biofuel and Biochemical Research, Department of Applied Sciences Universiti Teknologi PETRONAS, Seri Iskandar 32610, Perak Darul Ridzuan, Malaysia; junwei.lim@utp.edu.my
* Correspondence: cdho@mail.tku.edu.tw; Tel.: +886-2-26215656 (ext. 2724)

Abstract

Theoretical and experimental investigations were conducted to predict the permeate flux in double-pass air-gap membrane distillation (AGMD) modules operated with external recycle. These AGMD modules operate at moderate temperatures (40–55 °C) with a hot saline feed stream that is divided into two subchannels, while the cold inlet stream is maintained at a constant temperature. The temperature difference between the hot and cold streams establishes a gradient across the membrane surfaces and promotes the growth of thermal boundary layers, which gives rise to temperature polarization. To alleviate this problem, AGMD modules were fabricated in which the hot saline stream is split into a double-pass configuration by inserting an impermeable barrier; this strategy suppresses temperature polarization by enhancing the convective heat-transfer coefficient through the higher fluid velocity in each subchannel, thereby boosting the permeate flux and improving pure-water productivity. Various recycle ratios were implemented in the double-pass modules to optimize the heat-transfer characteristics and further mitigate temperature polarization. Theoretical predictions were validated against experimental results over a range of process parameters, including the inlet saline temperature, the volumetric flow rate, and the recycle ratio. Operating the AGMD modules in recycling double-pass mode provided a relative permeate-flux improvement of up to 82.51% at the highest recycle ratio compared with the single-pass module. Three-dimensional computational fluid dynamics (CFD) simulations of the feed subchannel ($Re_h = 116 \sim 610$), including a numerical residence-time distribution, showed that the distribution trenches supply the whole membrane width without stagnant zones (less than 4% of the membrane area below 10% of the mean velocity, mean residence time within 6% of the space time), and that the lateral flow maldistribution index lies between 0.16 and 0.41, the largest values occurring at the highest recycle-enhanced flow rates. The modeling equations confirm the technical feasibility of the proposed design, particularly for double-pass modules with external recycle in which an impermeable barrier is inserted into the saline feed stream.

Keywords: AGMD modules; permeate flux; Nusselt number; double-pass operation; temperature polarization; CFD; residence time distribution

Check for updates

Academic Editors: Efrem Curcio and Yuxi Huang

Received: 23 August 2026
Revised: 16 September 2026
Accepted: 25 November 2026
Published: 29 November 2026

Copyright: © 2026 by the authors. Licensee MDPI, Basel, Switzerland. This article is an open access article distributed under the terms and conditions of the Creative Commons Attribution (CC BY) license.

1. Introduction

Membrane distillation (MD) is a thermally driven separation process that has emerged as a promising alternative for desalination, solution concentration, and wastewater treatment, because it operates effectively at modest feed temperatures and near-atmospheric

hydrostatic pressures and is comparatively tolerant of fouling [1,2]. Continued progress in module design and process integration has steadily improved its prospects for industrial-scale deployment [3]. A key advantage of MD is its ability to utilize low-grade heat, especially when it is combined with solar heating systems or with waste heat from industrial processes. The temperature difference between the two membrane surfaces generates the vapor-pressure difference that drives the permeate flux: volatile species evaporate and are transported across a hydrophobic microporous membrane along this vapor-pressure gradient [4], and the process is therefore limited by heat-transfer resistance [5]. Compared with conventional packed-column processes, MD modules avoid common operational problems such as entrainment, flooding, channeling, and foaming [6], and they offer the practical advantage of integrating low-grade or waste-heat sources [7,8].

Despite these advantages, the performance of MD modules is constrained by temperature polarization, which diminishes the effective transmembrane temperature difference and consequently the permeate flux [9,10]. Mitigating this loss is a central design challenge, particularly at industrial scales, where polarization effects are amplified. Early work concentrated on quantifying the impact of temperature polarization on the permeate flux through hydrophobic membranes and on heat- and mass-transport modeling of various MD configurations [11], and the technical literature continues to place renewed emphasis on this challenge as the principal bottleneck to MD commercialization [12]. Numerous module-level strategies have been investigated, including spacer-filled channels [13], roughened or patterned surfaces [14], and carbon-fiber inserts [10], all of which act by disrupting the thermal boundary layer [15] and thereby reducing the temperature polarization coefficient (TPC) [16]. More recently, additively manufactured turbulence promoters of various geometries and hydraulic diameters have been shown to provide further gains in flux and energy utilization [17]. These enhancements, however, are typically accompanied by an undesirable rise in pressure drop, which must be weighed against the gain in permeate flux when economic feasibility is assessed [18,19]. Comprehensive reviews of MD module configurations [20] place these efforts within a broader trend toward energy-efficient, polarization-suppressing module designs that are essential for commercial viability.

A complementary strategy, drawn from the broader heat- and mass-transfer literature, is to introduce internal or external reflux into the flow channel. The use of recycle to raise the fluid velocity, and thereby the convective heat-transfer coefficient, has been investigated both theoretically and experimentally for parallel-plate and concentric-tube geometries since the late 1980s, where it is referred to as double-pass or double-flow operation. Analogous recycle schemes have been shown to improve heat- and mass-transfer rates in jet-loop reactors [21], air-lift reactors [22], and draft-tube bubble columns [23–25], all of which exploit internal or external reflux at one or both ends of the device. In the present study, the feed stream is divided into two subchannels separated by an impermeable barrier, and part of the exit stream is recycled back to the inlet, so that the convective velocity in each subchannel is increased without raising the net feed flow rate, thereby suppressing the thermal boundary layer at the membrane surface. In parallel, alternative process-level strategies have been investigated, including brine recycling for thermal-efficiency optimization in small-scale seawater desalination [26]. Such approaches are complementary to the present work in that they modify the operating mode of the module, whereas the recycle/reflux strategy considered here changes the flow arrangement, and hence the fluid velocity, in the feed channel inside a single-flow module. Within this framework, three design parameters consistently emerge as governing the trade-off between transfer enhancement and the additional power consumption introduced by recycling: the reflux (or recycle) ratio, the residence time, and the remixing effect that characterizes the entry-region behavior [27]. In the present study, the recycle ratio is varied experimentally, whereas the residence-time

behavior and the flow distribution in the feed channel are examined by three-dimensional CFD simulations (Sections 3.5 and 4.6). These three parameters, together with the choice between internal and external recycle, have not yet been developed for MD modules, in which phase change takes place at a hydrophobic membrane. Recent module-level studies have explored brine recycling [26] and membrane-surface modification for polarization suppression [28]; to date, however, no work has unified external recycling operations with MD applications [29].

The objective of the present work is to fill this gap by extending the double-pass air-gap membrane distillation (AGMD) framework [28] to incorporate the broader set of recycling configurations introduced here. Specifically, a unified theoretical and experimental analysis is developed for a flat-plate AGMD module operated under both internal- and external-recycle schemes, in which the recycle ratio is treated as an independent operating variable. Theoretical predictions are compared with experimental measurements of the permeate flux at various volumetric feed flow rates and inlet saline temperatures, and the relative gain in permeate flux is weighed against the incremental power consumption in order to identify economically attractive operating regions. The work thus provides a quantitative design tool for the joint optimization of these quantities within the practical setting of AGMD desalination modules, and clarifies when and how external recycle should be selected to maximize the permeate-flux enhancement. Earlier studies established the now-standard result that recycling operations can sharply improve heat- and mass-transfer rates, but at the cost of additional pressure drop and pumping power, so that the design problem reduces to identifying the operating points at which the gain in heat-transfer efficiency outweighs the incremental power consumption. The present study addresses this trade-off from the thermal side, through the effect of the double-pass flow arrangement and the recycle ratio on the convective heat-transfer coefficient, the temperature polarization and the permeate flux, and from the hydrodynamic side, through CFD simulations of the velocity field in the feed subchannel. This trade-off remains the organizing question for all subsequent work on recycling double-pass devices, including the present study.

These findings suggest that operating the modules with double-pass channels reduces the temperature polarization resistance and further enhances the permeate flux. The effect on the permeate flux was assessed using a dimensionless quantity, the heat-transfer enhancement factor, for which the heat-transfer coefficients were analyzed and expressed in terms of a correlated Nusselt number. This enhancement factor correlates the inlet hot saline feed temperature and the volumetric flow rate for various recycle ratios. The present work bridges the gap identified above by formulating numerical solutions for a recycling double-pass flat-plate AGMD module that admits both internal and external recycle, treats the recycle ratio as an independent design variable, and couples the energy balance to the vapor-pressure-driven permeate flux across the hydrophobic membrane. The resulting model recovers the limiting case of the single-pass AGMD configuration and extends it to a regime that has not previously been explored, thereby providing a unified design tool for AGMD modules with recycling double-pass operation. The findings demonstrate the technical feasibility and the potential advantages of the recycling double-pass design strategy presented in this study. The main contributions of this work are: (1) a one-dimensional model of the double-pass AGMD module with external recycle, validated against permeate-flux measurements at four inlet saline temperatures, four volumetric flow rates and several recycle ratios, with mean deviations below 10%; (2) a correlation of the heat-transfer enhancement factor in terms of the recycle ratio, Reynolds number and Prandtl number; (3) a quantification of the permeate-flux improvement (up to 33.91% for $R = 0$ and 82.51% for $R = 0.75$ relative to the single-pass module) together with the associated hydraulic power penalty, expressed through the ratio I_N/I_P; and (4) a three-dimensional CFD

assessment of the hydrodynamics of the double-pass subchannel, including velocity fields, a flow-maldistribution index and a numerical residence-time distribution, which identifies stagnant zones and channeling, quantifies the deviation from the plug-flow assumption of the model and shows how it depends on the recycle-enhanced flow rate.

2. Experimental Setup and Materials

2.1. Design of Double-Pass Modules

The experimental setup comprised two parallel-plate channels (dimensions: 0.21 m length, 0.29 m width, 2 mm channel height for each cold and hot feed stream, and air-gap channel) divided by a hydrophobic composite membrane constructed from PTFE/PP (polytetrafluoroethylene and polypropylene, J020A330R, ADVANTEC, Toyo Roshi Kaisha, Ltd., Tokyo, Japan). The microporous hydrophobic membrane has a nominal pore size of 0.2 μm, porosity of 0.72, and an overall thickness of 130 μm (composed of 98 μm PTFE and 32 μm PP), serving as the medium for vapor flux permeation, which has a thermal conductivity of 0.21 W/m K (All-Fluoro Co., Ltd., Taoyuan, Taiwan) and the water vapor permeability resistance of 4 s/m [30]. Silicon rubber gaskets (2 mm thick) were affixed to acrylic plates to prevent leakage and form spacer conduits. The schematic design and construction specifics of the flat-plate AGMD module featuring two-flow conduits of the hot saline channel were assessed using a flat-plate experimental configuration, and a silicone rubber gasket with a thickness of 2 mm was bonded to the acrylic plate to define the spacer channel and prevent leakage, as depicted in Figure 1. The schematic configuration and fabrication details of the double-pass flat-plate AGMD module incorporating two flow channels are illustrated in Figure 1. The machining details of the double-pass AGM module with acrylic plates serving as the outer walls of the parallel-plate structure are shown in Figure 2a,b. The machining process for fabricating those two channels was first designed using CAD digital graphic images and processed by CNC milling cutter machines. Figure 2a provides a graphical representation of digging a trench with a semicircular cross-section for the double-pass AGMD module in the hot saline feed channel, tailored precisely to the manufacturing process requirements. The experiments were conducted to control various feed flow rates regulated by a rotameter, with the feed pumped equally from a thermostat, and the feed stream overflows the semicircular trench through the 2 mm channel. These visuals provide a clear representation of the experimental setup and configuration used in the study.

The hydrophobic membrane surfaces were supported by embedding the spacer structure by inserting straight carbon-fiber spacers near the membrane surface in the air-gap channel to prevent membrane bending and wrinkling for mechanical reinforcement. All carbon-fiber spacers occupied approximately 13% of the hydrophobic membrane surface area with assuming not affect the vapor transferring mechanism in the air-gap conduit, which possess a tensile strength of 3530 MPa and thermal conductivity of 10.5 W/m K (TORAY T300B, San Li Composites, Co., Ltd., Taichung, Taiwan) with its rigidity, chemical resistance, and negligible thermal resistance, as shown in Figure 3. Comparative evaluations were conducted across various operating conditions between flat-plate membrane distillation modules under single-pass and double-pass configurations. This study presents a mathematical model of permeate flux in the hot saline feed channel of the flat-plate membrane distillation module, permeate flux transferring in the air-gap channel, and the cold feed stream flowing through an adjacent channel, as shown in Figure 4, within a photo of the operating experimental apparatus, where the acrylic plates functioning as the exterior walls of the parallel-plate assembly are stacked as the outer walls of the parallel-plate channel.

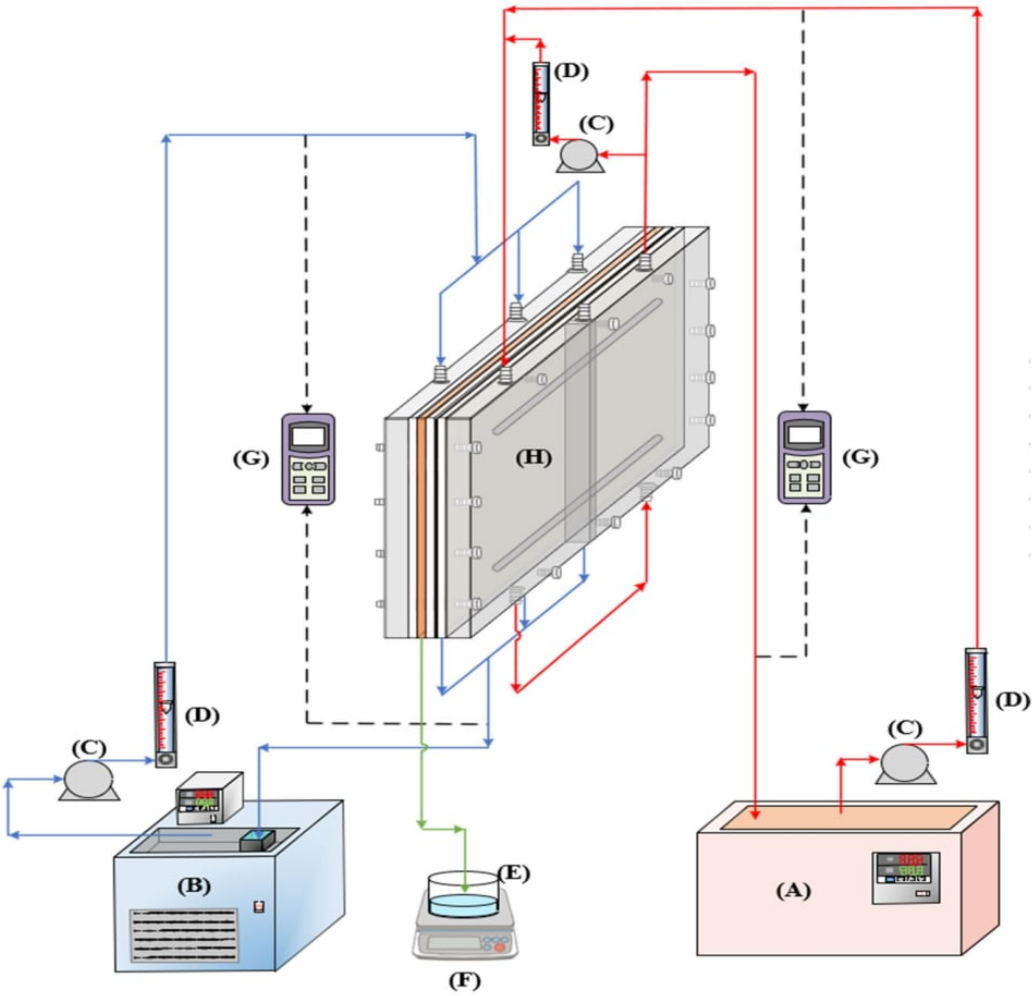
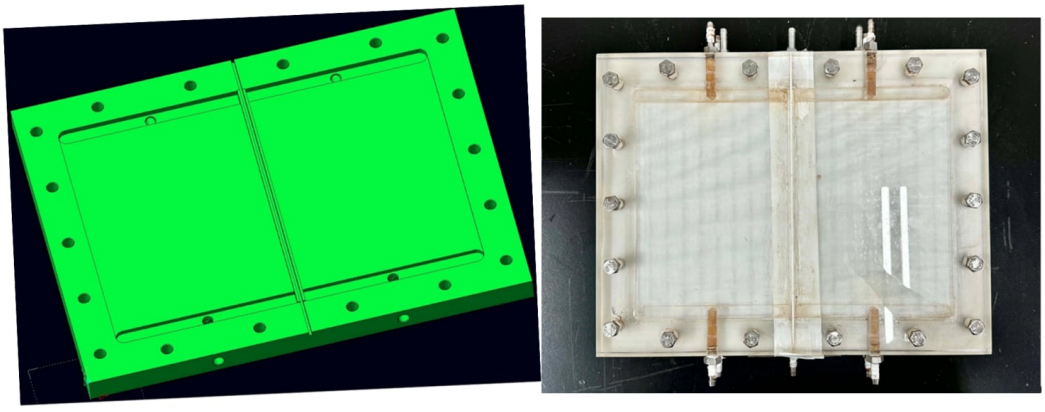


Figure 1. Scheme of a setup used in experiments of flat-plate AGMD modules (A—Hot fluid thermostat; B—Cold fluid thermostat; C—Pump; D—Flow meter; E—Beaker; F—Electric balance; G—Temperature indicators; H—Double-pass AGMD module).



(**a**) CAD digitalized graphic image (**b**) Photographic image

Figure 2. Double-pass AGMD channels.

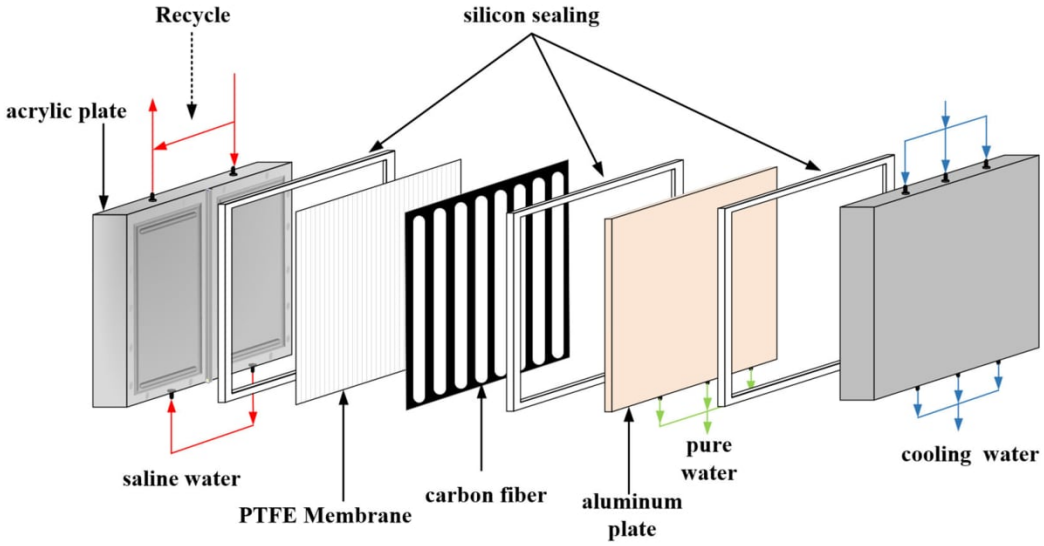


Figure 3. Components of the double-flow flat-plate AGMD module.

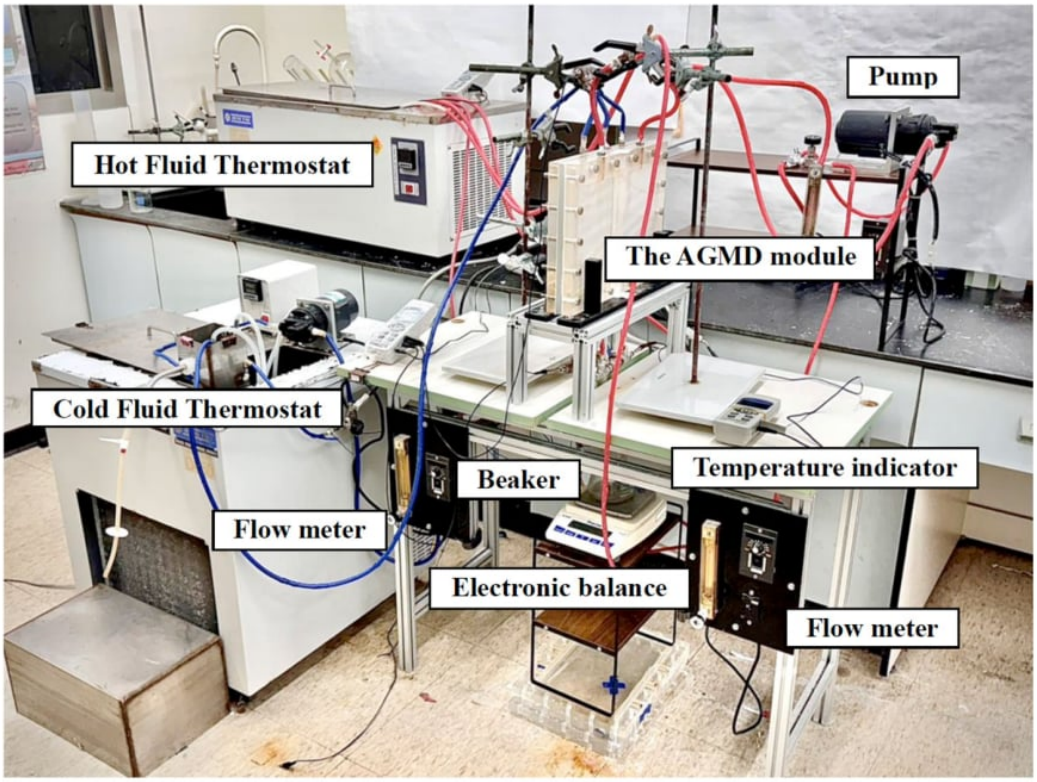


Figure 4. A photo of the experimental apparatus of the double-pass AGMD system (side view).

2.2. Air-Gap Membrane Distillation Experiments

Artificial saline feed water with a 3.5 wt% NaCl concentration was prepared by dissolving inorganic NaCl in distilled water. Experimental runs of various flow rates of 0.3, 0.5, 0.7, 0.9 L min^{-1} (say 5.0×10^{-6}, 8.33×10^{-6}, 1.17×10^{-5}, and 1.5×10^{-5} m^3 s^{-1}) of artificial saline water at inlet hot saline feed temperatures of 40, 45, 50, and 55 °C, with the cold feed stream maintained at 25 °C under the same flow rates as the hot feed stream, which were regulated using using rotameters (FE-091312-D for the hot stream; FN-0423112-F for the cold stream; Fong-Jei, Hsinchu, Taiwan) and a controller (US-2000-40W, ASTK, New Taipei, Taiwan). The temperatures of both streams were supplied by two thermostats (G-50, 60 L,

3500 W; DENG YNG, Kaohsiung, Taiwan) and circulated through the flat-plate module using conventional pumps (51K40RA-A, ASTK, New Taipei, Taiwan) to maintain steady inlet temperatures for the two streams. Inlet and outlet temperatures were monitored using thermometer probes (TM-946, Lutron, New Taipei, Taiwan) installed on both sides of the flat-plate membrane modules until the system reached steady-state conditions. The repeatability of pure water conductivity measurements was always within 5%, enabling reliable determination of vapor permeate flux. Permeate vapor condensed in the cold stream was collected and weighed using an electronic balance (XS 4250C, Precisa Gravimetrics AG, Dietikon, Switzerland), and the measured pure water was recorded via a PC. Meanwhile, a conductivity meter (CD-4303, Lutron Electronic Enterprise Co., Ltd.) was employed to monitor changes in the conductivity of the collected permeate [31]. All experiments were conducted with the hot saline feed stream in one-through operations, and the reproducibility of the permeate flux measurements was mostly within 5%, allowing for further determination of the device performance to confirm water purity with values consistently below 2.0 µs/cm.

2.3. Characterization

The implementation of double-flow channels significantly enhanced the convective heat-transfer coefficient within the saline feed channel. This effect was particularly pronounced in modules utilizing recycling double-pass configurations, which contributed to improved heat transfer rate and increased permeate flux. Comparative analyses of permeate flux were conducted under various operating conditions to evaluate the performance of two AGMD modules—the implementation of single- and double-pass operations. The operating conditions and specifications of the AGMD module used are summarized in Table 1. The SEM images obtained via high-energy electron beams confirmed that the PTFE/PP membranes exhibited no fouling or swelling [32], verifying their structural stability and chemical resistance. The morphology and water contact angles of the PTFE/PP composite membranes were characterized during experimental runs. Surface and cross-sectional morphologies [33] of both fresh and used membranes were examined by scanning electron microscopy (SEM, Zeiss Sigma 300, Jena, Germany), as shown in Figure 5.

Table 1. Property specifications and operation parameters.

Specifications/Parameter	Value
Membrane pore size (diameter)	0.2 µm
Porosity	0.72
Thickness	130 µm (98 µm PTFE and 32 µm PP)
Inlet hot saline feed temperature	40, 45, 50, and 55 °C
Inlet cold feed temperature	25 °C
Configurations	Single-, double-, and recycling double-pass operations
Feed NaCl concentration	3.5 wt%
Membrane thermal conductivity	0.21 W $m^{-1}K^{-1}$
Membrane permeability resistance	4 s/m
Carbon-fiber tensile strength	3530 MPa
Carbon-fiber thermal conductivity	10.5 W $m^{-1}K^{-1}$
Hot and cold volumetric flow rates	0.3, 0.5, 0.7, 0.9 L min^{-1}
Permeate conductivity	below 2.0 µs/cm
Channel size	0.21 m length, 0.29 m width, 2 mm height
Contact angle	116–124°

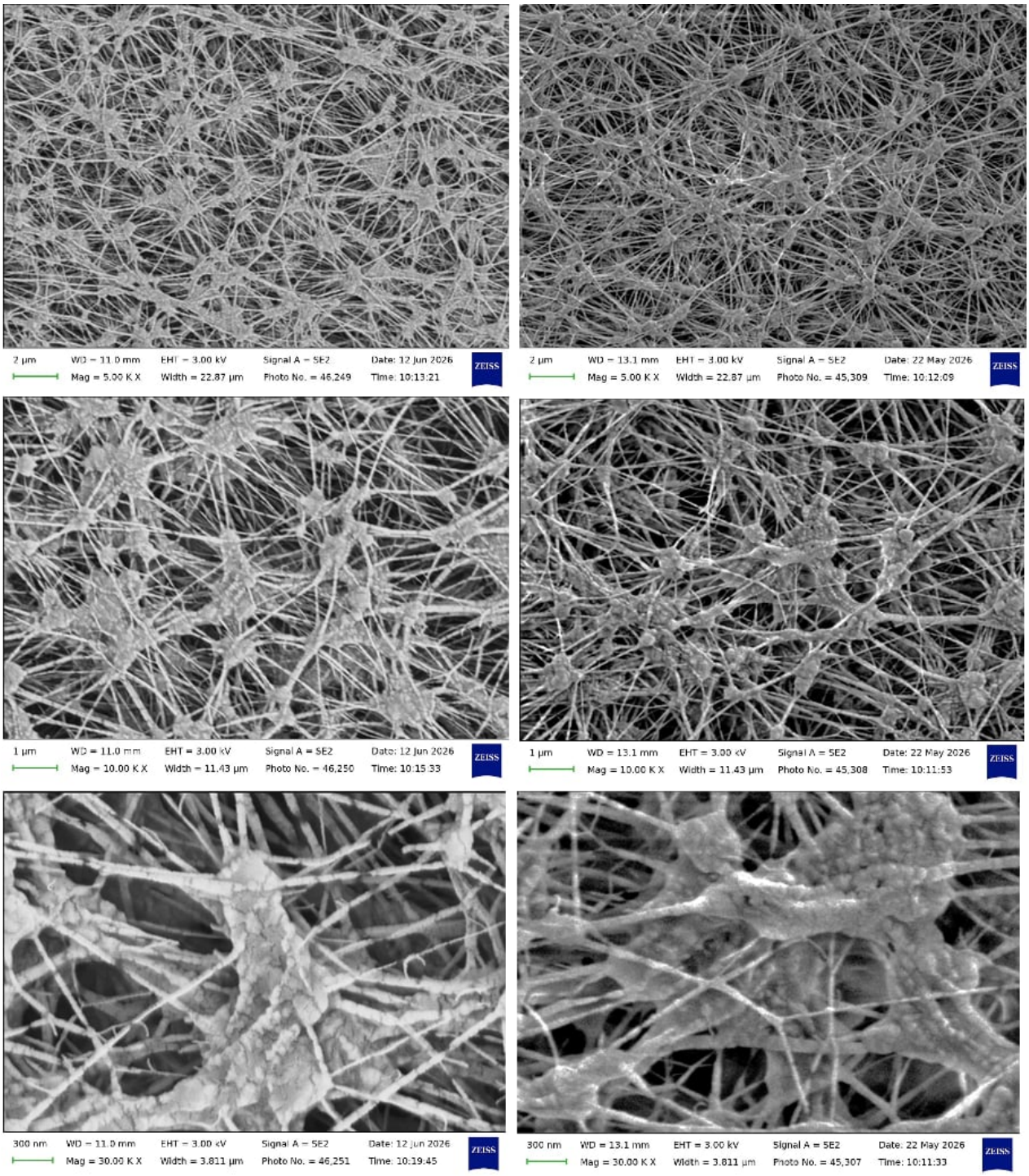


Figure 5. SEM images of fresh and used PTFE/PP membranes of experimental runs.

The water contact angles of the PTFE/PP composite membranes were further investigated using an optical contact angle measuring instrument (First Ten Angstrom FTA-125; Portsmouth, VA, USA) to confirm surface hydrophobicity [34]. As shown in Figure 6, the contact angles ranged from 116 to 124° (122 ± 4.0°) to confirm the hydrophobic nature of the membrane. All characterizations were conducted with multiple validations to ensure the accuracy and reliability of the results. No flux decline, conductivity increase, or morphological change of the membrane was detected over the cumulative operating time of the experiments; long-term stability beyond this period was not assessed in the present study.

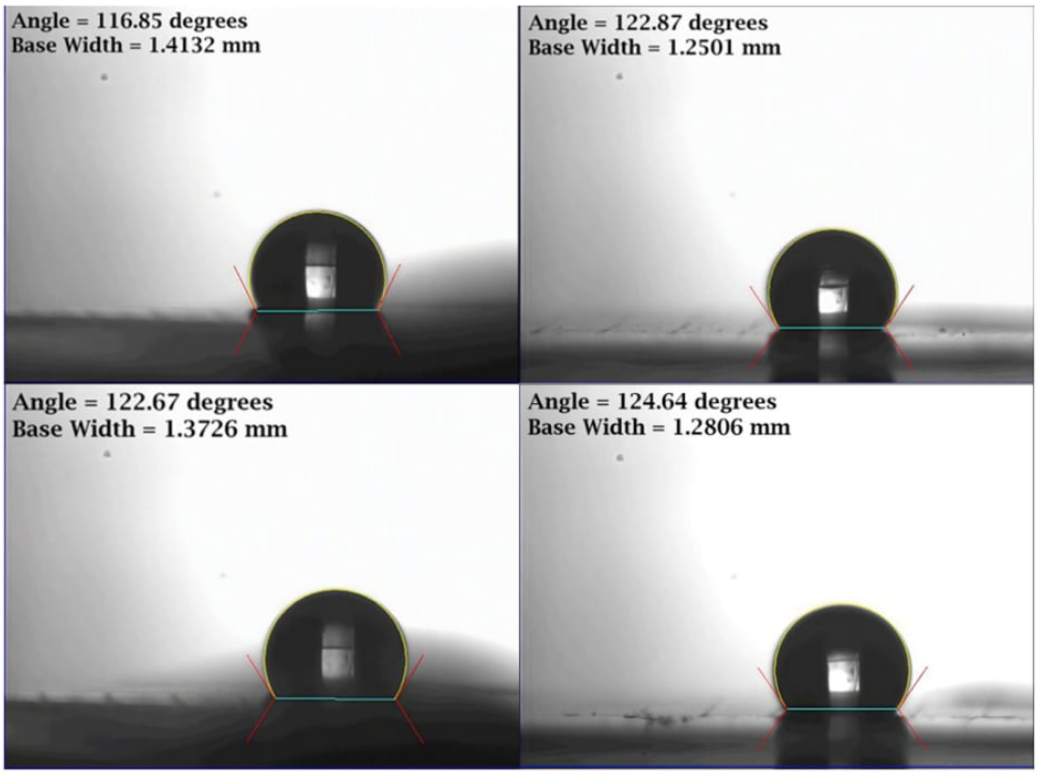


Figure 6. Sessile-drop contact angles of PTFE/PP membranes.

3. Theory and Analysis

3.1. Heat and Mass Transfer

A theoretical formulation coupling the complex interplay between simultaneous heat and mass transfer mechanisms according to vapor–liquid thermodynamic equilibrium for the AGMD system, as illustrated in Figure 6, was developed, which developed a mass-balance model for water vapor transferring in the hot saline feed channel, diffusing exclusively through microporous hydrophobic membranes, transporting in the air-gap channel, and then condensing on the cooling plate surface and producing pure water in such a membrane distillation process.

A heat-transfer balance equation was applied to quantify the amount of vapor generated in the hot saline feed stream, while a mass-transfer balance was used to determine temperature changes at both membrane surfaces resulting from permeate flux transfer. The membrane distillation coefficient is the combination of the Knudsen diffusion coefficient, the molecular diffusion coefficient, and the viscous flow coefficient. However, the value of the viscous flow coefficient among the three coefficients was calculated and found to be negligible under the operating conditions in the present study. To estimate the permeate flux, an expression for the membrane permeation coefficient (c_m) was used, which combines the effects of Knudsen and molecular diffusion, as appropriate for microporous hydrophobic membranes [35]. The product of the membrane permeation coefficient (c_m) and the transmembrane vapor pressure difference (ΔP) has been widely utilized in mass-transfer analyses of permeate flux in membrane distillation systems [36]. The approximate solution of membrane distillation equations may be obtained by employing simplifying assumptions. The Clausius–Clapeyron equation was used to simplify the vapor pressure-temperature relationship with the use of the saturation pressure and the molar latent heat of vaporization when the temperature gradient $\Delta T < 15$ °C [1]. For the nominal pore diameter of 0.2 μm, the mean free path [1] of water vapor in air gives $\lambda_{fp} = 0.102 \sim 0.111$ μm at $30 \sim 55$ °C and $\mathrm{Kn} = \lambda_{fp}/d_p = 0.51 \sim 0.55$. Vapour transport in the pores therefore lies in the Knudsen

molecular transition region, and both mechanisms are retained in Equation (3); the Knudsen resistance accounts for 70 ~ 90% of the membrane resistance ($c_k = 1.12 \times 10^{-6}$ and $c_M = 0.77 \sim 0.95 \times 10^{-6}$kgm^{-2}s^{-1}Pa^{-1}). Viscous (Poiseuille) flow does not occur, because the total gas pressure is atmospheric on both faces of the membrane.

Balances of permeate flux conservation with the vapor–liquid equilibrium assumption, encompassing both mass diffusion and enthalpy flow associated with heat conduction, were formulated simultaneously as follows.

$$N'' = c_T \Delta P = c_T \left[P_1^{sat}(T_1) - P_3^{sat}(T_3) \right] = c_T \left. \frac{dP}{dT} \right|_{T_m} (T_1 - T_3) = c_T \frac{P_m \lambda M_w}{R_c T_m^2} (T_1 - T_3) \quad (1)$$

and

$$c_T = \left(\frac{1}{c_m} + \frac{1}{c_a} \right)^{-1} = \left[\left[\frac{2}{3} \frac{\varepsilon r}{\tau_m \delta_m} \sqrt{\frac{8}{\pi}} \left(\frac{M_w}{R_c T_m} \right)^{\frac{1}{2}} \right]^{-1} + \left[\frac{1}{|Y_m|_{ln} \frac{D_m \varepsilon}{\delta_m \tau_m} \frac{M_w}{R_c T_m}} \right]^{-1} + \left[\frac{1}{|Y_a|_{ln} \frac{D_a}{\delta_a} \frac{M_w}{R_c T_a}} \right]^{-1} \right]^{-1} \quad (2)$$

in which

$$\boldsymbol{c_m = \left(\frac{1}{c_K} + \frac{1}{c_M} \right)^{-1} = \left\{ \left[\frac{2}{3} \frac{\varepsilon r}{\tau_m \delta_m} \sqrt{\frac{8}{\pi}} \left(\frac{M_w}{R T_m} \right)^{1/2} \right]^{-1} + \left[|Y_m|_{ln} \frac{D_m \varepsilon}{\delta_m \tau_m} \frac{M_w}{R T_m} \right]^{-1} \right\}^{-1}} \quad (3)$$

and

$$|Y_m|_{ln} = \frac{(P_T - P_2) - (P_T - P_1)}{P_T ln\left[\frac{((P_T - P_2))}{((P_T - P_1))} \right]}, \quad |Y_a|_{\ln} = \frac{(P_T - P_2) - (P_T - P_3)}{P_T * \ln\left[\frac{(P_T - P_2)}{(P_T - P_3)} \right]}, \tau_m = \frac{1}{\varepsilon}, D_m = \frac{1 \times 10^{-7} T_m^{1.75}}{\frac{P_T}{101{,}325} M_{w-air}^{0.5} \left(\sigma_w^{1/3} + \sigma_{air}^{1/3} \right)^2},$$
$$D_a = \frac{1 \times 10^{-7} T_a^{1.75}}{\frac{P_T}{101{,}325} M_{w-air}^{0.5} \left(\sigma_w^{1/3} + \sigma_{air}^{1/3} \right)^2}, M_{w-air} = \left[\left(\frac{1}{M_w} \right) + \left(\frac{1}{M_{air}} \right) \right]^{-1} \quad (4)$$

The temperature was calculated using the Antoine equation and T_m was the average temperature calculated by T_1 and T_3 to incorporate into the derivative $\left. \frac{dP}{dT} \right|_{T_m}$ in Equation (1). The saturation vapor pressure $P_1^{sat}(T_1)$ of the hot feed stream can be estimated using the water activity coefficient a_w, for which a correlation was determined [37] as:

$$P_1^{sat}(T_1) = y_w P = x_w a_w P_w^{sat} \quad (5)$$

$$a_w = 1 - x_{NaCl} - 10 x_{NaCl}^2 \quad (6)$$

and the tortuosity (τ) can be estimated using the porosity of the membrane [38]

$$\tau_m = 1/\varepsilon \quad (7)$$

Under steady-state operation, the energy balance equations for each heat-transfer region were derived according to the schematic diagram of the AGMD module using the conservation of enthalpy flow, considering both conduction heat flow, mass diffusion enthalpy flow, and the latent heat of vaporization $N''\lambda$ through the composite system [35], as shown in Figure 7.

Vapor permeate diffuses exclusively through the hydrophobic membrane in the membrane distillation process, where the bulk temperatures of the feed streams are denoted as $T_{h,1}$ and $T_{h,2}$ (both subchannels of the hot saline feed stream) and T_c (the cold feed stream) in the recycling double-pass AGMD module with external recycle, as shown in Figure 8a,b.

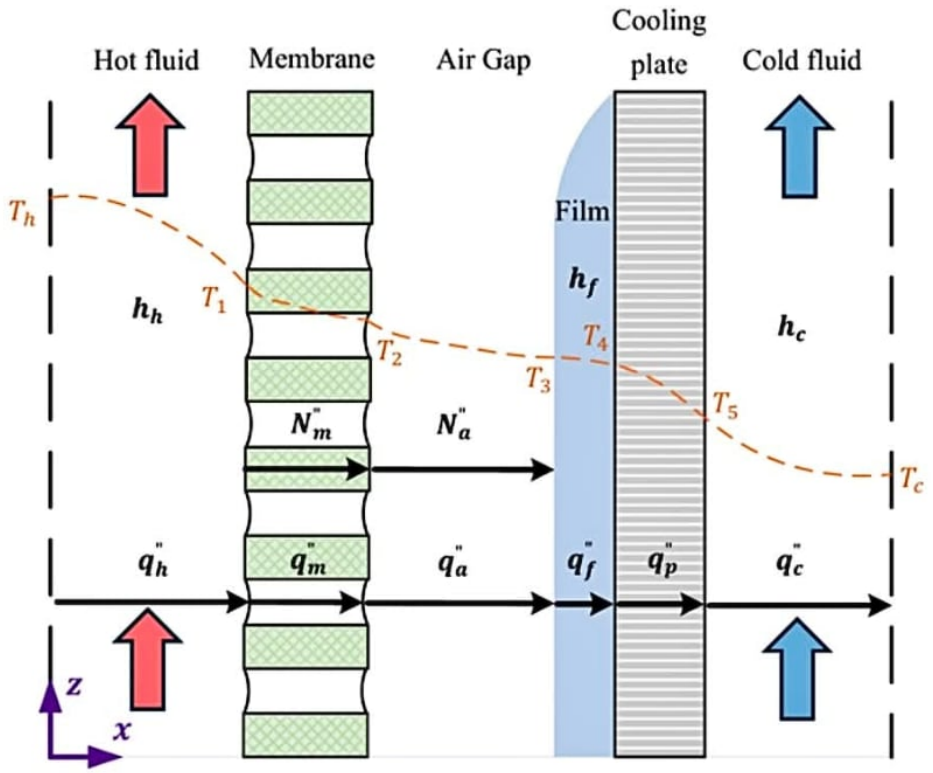


Figure 7. Heat transfer mechanisms and thermal boundary layer in the AGMD module.

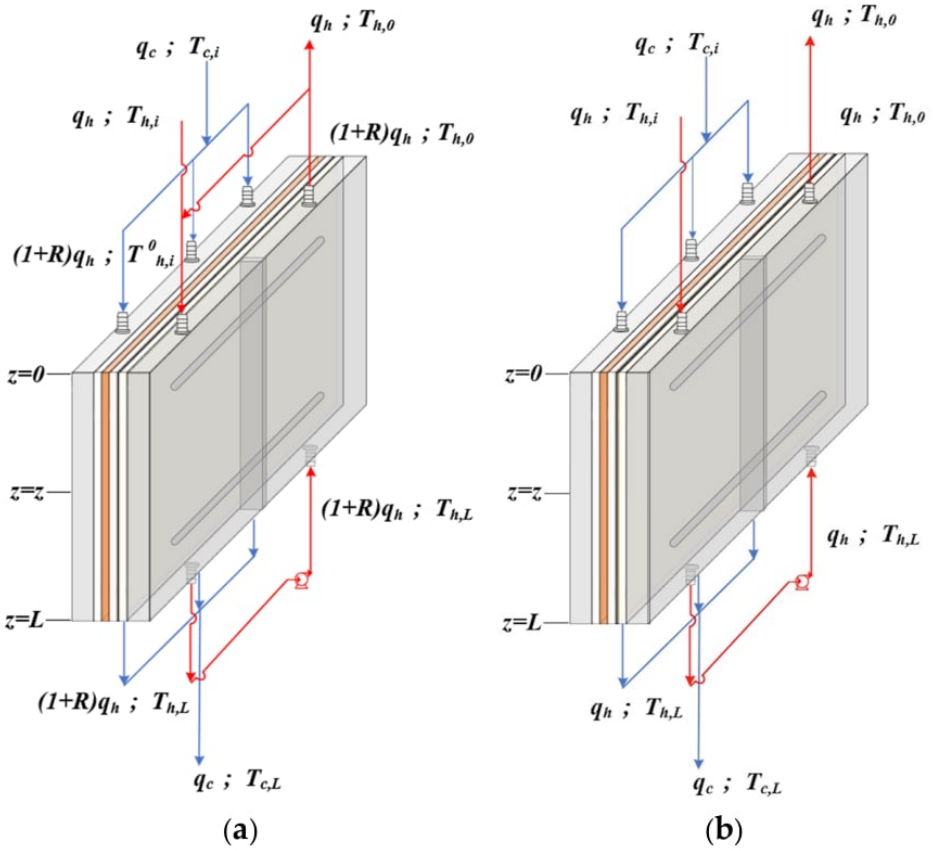


Figure 8. Recycling double-pass AGMD module with external recycle (Blue line: cold feed stream, Red line: hot feed stream) (**a**) Recycling double-pass configurations; (**b**) Double-pass configurations with internal recycle ($R = 0$).

Before entering the left-hand-side channel for a recycling double-pass operation as shown in Figure 8a, the fluid with volumetric flow rate q_h and the inlet temperature $T_{h,i}$ from the left-hand-side channel will mix with the fluid of volumetric flow rate Rq_h and the outlet temperature $T_{h,0}$ from the right-hand-side channel, which is regulated by using a conventional pump. The fluid is completely mixed at the inlet and outlet of the channel. According to Figure 7, vapor permeate diffuses exclusively through the hydrophobic membrane in the membrane distillation process. The heat transfer mechanisms in the AGMD system caused by the temperature gradient across each component of the module were presented in Equations (8)–(14) as follows:

$$q''_{h,1} = \frac{1}{2}h_{h,1}(T_{1,1} - T_1), \text{ left-hand-side subchannel} \tag{8a}$$

$$q''_{h,2} = \frac{1}{2}h_{h,2}(T_{1,2} - T_1), \text{ right-hand-side subchannel} \tag{8b}$$

$$q''_m = \left[N''\lambda + \frac{k_m}{\delta_m}\ (T_1 - T_2)\right], \text{ membrane region} \tag{9}$$

$$q''_a = N''\lambda + \frac{k_a}{\delta_a}\ (T_2 - T_3), \quad \textit{air gap region} \tag{10}$$

The two subchannels are connected in series through the external line shown in Figure 8a, so that the same flow rate $(1 + R)q_h$ passes through both of them by continuity; the factor $1/2$ represents the fraction of the membrane area (width $W/2$) facing each subchannel, not a division of the flow. Non-uniform velocity across the subchannel width affects the total flux only to second order; for a $\pm 20\%$ lateral imbalance, the predicted flux changes by less than 0.5%. As the vapor flux reaches the condensation surface, it condenses and forms a condensate film [39], and the condensation would be filmwise. Meanwhile, no flooding of water and the condensate film covering the entire condensation surface were assumed. This condensate film forms a heat transfer resistance that can be expressed as [40].

$$q''_f = h_f(T_3 - T_4) = 0.943\left[\frac{\rho^2 g\lambda {k_f}^3}{\mu L(T_3 - T_4)}\right]^{\frac{1}{4}}(T_3 - T_4), \text{ condensate film} \tag{11}$$

$$q''_p = \frac{k_p}{\delta_p}\ (T_4 - T_5), \text{ condensing plate} \tag{12}$$

$$q''_c = h_c(T_5 - T_c), \text{ cold feed stream} \tag{13}$$

The cooling plate is vertical with height $L = 0.21$ m. With the film mass flow per unit width at the bottom edge $\Gamma = N''L$, the film Reynolds number $\mathrm{Re}_f = 4\Gamma/\mu$ is $1.0 \sim 2.7$ for all operating conditions, far below the onset of waviness ($\mathrm{Re}_f \approx 30$) and of turbulence ($\mathrm{Re}_f \approx 1800$) [41], so the laminar Nusselt film model applies. The maximum film thickness from the Nusselt solution is $34 \sim 48$ μm ($\leq 2.4\%$ of the air gap), and the film contributes less than 2% of the overall heat-transfer resistance. Equating the energy conservation of heat fluxes for three combined intervals, $(T_h - T_1)$, $(T_1 - T_3)$ and $(T_3 - T_c)$, say q''_h, q''_{ma} and q''_{fc}, respectively, as shown in Figure 7, leads to the overall heat transfer coefficient of the hot feed stream, membrane region, and cooling stream, respectively.

$$q''_h = q''_{h,1} + q''_{h,2} = \frac{1}{2}h_{h,1}(T_{1,1} - T_1) + \frac{1}{2}h_{h,2}(T_{1,2} - T_1), \text{ hot saline feed stream} \tag{14}$$

$$\begin{aligned} q''_{ma} &= q''_m + q''_a = N''\lambda + \left[\frac{\delta_m}{k_m} + \frac{\delta_a}{k_a}\right]^{-1}(T_1 - T_3) \\ &= \left\{c_T \frac{[(1-x_{\mathrm{NaCl}})(1-0.5x_{\mathrm{NaCl}}-10x_{\mathrm{NaCl}}^2)P_w^{sat}+P_3^{sat}]\lambda^2 M_w}{2RT_{avg}^2} + \left(\frac{k_m}{\delta_m} + \frac{k_a}{\delta_a}\right)^{-1}\right\}(T_1 - T_3) \\ &= H_m(T_1 - T_3), \text{ membrane region} \end{aligned} \tag{15}$$

and

$$q''_{fc} = \left[\frac{1}{h_f} + \frac{\delta_p}{k_p} + \frac{1}{h_c}\right]^{-1}(T_3 - T_c) = H_c(T_3 - T_c), \text{ cold feed stream} \quad (16)$$

where H_m is the heat-transfer coefficient of the interval $(T_1 - T_3)$, $N''\lambda$ is characterized as the latent heat, and $\frac{k_m}{\delta_m}$ and $\frac{\delta_a}{k_a}$ are the conductive heat transfer coefficients. Air-gap resistance in the AGMD module is the mass-transfer resistance imposed by the stagnant air layer between the membrane surface and the cooling plate, and the dominant resistance accounts for roughly 70–90% of the total mass-transfer resistance. A typical air-gap thickness is of 1~5 mm to neglect the convection inside the air gap's influence [42], with an air gap of 2 mm being less than 5 mm for conducting the experimental runs. The air gap is also a thermal insulator to suppress conductive heat loss and raise thermal efficiency. Treating the air gap as a vertical enclosure (height 0.21 m, width 2 mm), the Rayleigh number based on the combined thermal and solutal density difference is $\mathrm{Ra}_\delta = 3 \sim 14$, far below the value of order 10^3 at which natural convection begins in tall vertical air layers [43]. Heat and vapor therefore cross the air gap by conduction and diffusion only, as expressed by Equations (2) and (10). The thermal conductivity of the membrane k_m can be calculated by the thermal conductivities of vapor in the membrane pore k_g and the solid membrane material k_s by Warner [44] as:

$$k_m = \varepsilon k_g + (1 - \varepsilon)k_s \quad (17)$$

The heat transfers across the hot saline feed stream, membrane, and cold feed stream should be balanced as $q''_h = q''_m = q''_a = q''_{ma} = q''_f = q''_p = q''_c = q''_{fc}$, and the heat transfers across the hot saline feed stream, membrane region, and cold feed stream should be balanced using Equations (8a,b), (15) and (16) as follows:

$$\frac{1}{2}h_{h,1}(T_{1,1} - T_1) + \frac{1}{2}h_{h,2}(T_{1,2} - T_1) = H_m(T_1 - T_3) = H_c(T_3 - T_c) \quad (18)$$

The heat transfer through the hot side, hydrophobic membrane, and cold side should be balanced by solving Equation (18) with respect to $T_{1,1}$, $T_{1,2}$, and T_c, one gets

$$T_{1,1} = \frac{h_h T_{h,1}\left[(H_c + H_m)\left(h_h + \frac{1}{2}H_m\right) + \frac{1}{2}H_m H_c\right] + \frac{1}{2}H_m^2 h_h T_{h,2} + H_m H_c T_c(h_h + H_m)}{(h_h + H_m)[h_h(H_c + H_m) + H_c H_m]} \quad (19)$$

$$T_{1,2} = \frac{h_h T_{h,2}\left[(H_c + H_m)\left(h_h + \frac{1}{2}H_m\right) + \frac{1}{2}H_m H_c\right] + \frac{1}{2}H_m^2 h_h T_{h,1} + H_m H_c T_c(h_h + H_m)}{(h_h + H_m)[h_h(H_c + H_m) + H_c H_m]} \quad (20)$$

$$T_c = \frac{T_3(H_c + H_m) - \frac{1}{2}H_m(T_{1,1} + T_{1,2})}{H_c} \quad (21)$$

The thermal boundary layers of both water and air channels play an important role in determining the permeate flux and are commonly expressed as the temperature polarization coefficient [35] in the device performance of the AGMD module, which controls the permeate flux through the membrane γ_m is commonly in the single-pass operation defined as:

$$\gamma_m = (T_1 - T_3)/(T_h - T_c) \quad (22)$$

Based on Equations (19)–(21), the schematic diagram in Figure 7 illustrates all heat transfer regions at the microscopic level under steady-state operation. The temperature polarization coefficients $\gamma_{m,1}$ and $\gamma_{m,2}$ of the present double-flow modules are defined as:

$$\gamma_{m,1} = \frac{(T_1 - T_3)}{(T_{h,1} - T_c)} = \frac{h_{h,1}H_c}{h_{h,1}H_c + h_{h,1}H_m + H_c H_m} \quad (23)$$

$$\gamma_{m,2} = \frac{(T_1 - T_3)}{(T_{h,2} - T_c)} = \frac{h_{h,2}H_c}{h_{h,2}H_c + h_{h,2}H_m + H_c H_m} \quad (24)$$

The permeate flux was estimated and calculated from Equation (1), and validated by the experimental results by iterating $T_{1,1}$, $T_{1,2}$ and T_c incorporating initial guesses of $h_{h,1}$ and $h_{h,2}$ from Equations (19)–(21) until reaching the convergence tolerance.

3.2. Theoretical Analyses of the Heat Transfer and Mass Transfer

A novel design of an air-gap membrane distillation (AGMD) module was proposed that introduces an insulation barrier of negligible thickness to divide the open conduit of the hot saline feed stream into two subchannels with the same width of $W/2$ and that a pump is installed for recycling flow with recycle ratio R. Moreover, the most important assumption is that the fluid temperatures and velocities in the flow direction of both hot saline and cold feed streams are uniform over cross sections along the flow channels and that a plug-flow description is used in mathematical modeling. The one-dimensional mathematical formulation equations were derived by constructing the permeate flux diagram in a finite control element according to the heat conservation law under steady-state operations, with the coordinate along the z-axis representing the flow direction. The schematic diagram of the plug-flow description considers only the largest temperature gradient in the heat-transfer balance equation, neglecting all diffusion terms, as shown in Figure 9.

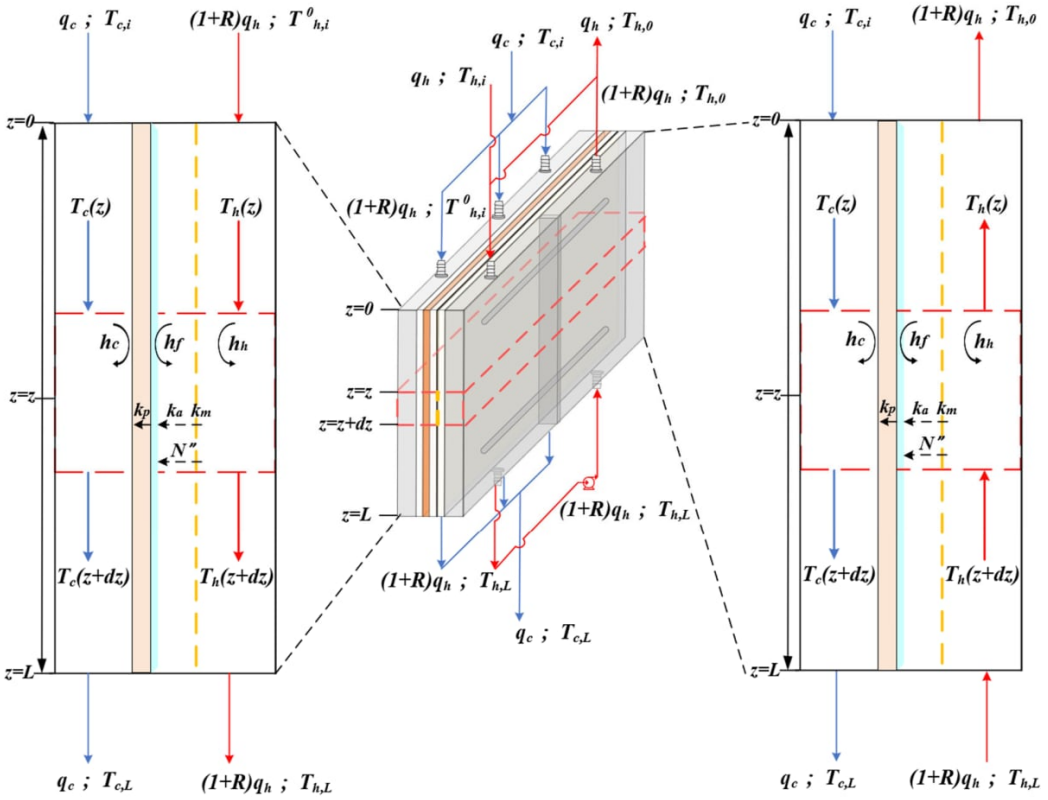


Figure 9. The energy balance made by using the plug-flow description within a finite fluid element in a recycling double-pass AGMD module (Yellow line: membrane).

This approach is also associated with the most simplified macroscopic description for both hot saline and cold feed streams. The assumptions used in this mathematical model include the following: (1) the recycling double-pass AGMD system operates under steady-state conditions; (2) the membrane properties are uniform; (3) the permeate vapor fills the membrane pores; (4) non-wetting conditions for the membranes; (5) fluid physical properties are constant; (6) negligible axial diffusion and conduction compared to convection; (7) the condensate forms a thin liquid film and covers the entire cooling plate surface; (8) the entire recycling double-pass AGMD module is insulated except across the heat-transfer

membrane; (9) neglect of fouling; (10) no internal generation of energy; and (11) well mixing at both inlet and outlet of each channel. For $87.8 \leq Re_h \leq 572.7$ the hydrodynamic entrance length $L_{e,h} = 0.035\, Re_h D_{h,h}$ [45] is 1.2 ~ 7.9 cm, i.e., up to 38% of the channel length, and the thermal entrance length ($\approx 0.05\,\mathrm{RePr}D_{h,h}$) exceeds the channel length at the higher flow rates. The flow is therefore thermally developing; this is accounted for through the length-averaged heat-transfer coefficients of Equations (35) and (36), which were regressed from full-length module measurements and are valid only within the present geometry and Reynolds-number range. Axial conduction is negligible because $\mathrm{Pe} = \mathrm{RePr} = 290 \sim 2460 > 100$ [25]. The plug-flow description assumes that each subchannel is swept uniformly. Taylor [46] showed for laminar flow that a process of mass transfer may be equally well described by flow with a flat velocity profile over the entire cross section of the module equal to the actual mean velocity, in which each element of fluid that enters the module marches through in single file without intermingling with other fluid. The two subchannels are connected in series, so the same flow rate passes through both by continuity, and axial back-mixing is negligible ($\mathrm{Pe} > 100$). Lateral non-uniformity across the channel width affects the total flux only to second order (less than 0.5% for a ±20% imbalance). The validity of this description for the present module, including possible stagnant zones near the inlet and outlet ports and channeling, is assessed by the three-dimensional CFD simulations of Sections 3.5 and 4.1. The deviations between predicted and measured permeate fluxes remain below 10% over all operating conditions in Section 4.4; the slight over-prediction observed at the higher flow rates is consistent with the larger lateral flow maldistribution found by CFD at the highest flow rates.

The equations of energy thus may be obtained to solve the temperature distributions of both hot saline and cold feed streams in terms of the temperature polarization coefficients, $\gamma_{m,1}$ and $\gamma_{m,2}$, as described below:

$$(1+R)m_h \frac{dT_{h,1}(z)}{dz} = -\left(\frac{W}{2}\right) H_m \gamma_{m,1}\left(T_{h,1} - T_c\right) \tag{25}$$

$$(1+R)m_h \frac{dT_{h,2}(z)}{dz} = \left(\frac{W}{2}\right) H_m \gamma_{m,2}\left(T_{h,2} - T_c\right) \tag{26}$$

$$m_c \frac{dT_c(z)}{dz} = W H_m \gamma_{m,2}\left(T_h - T_c\right) \tag{27}$$

where m_h $\left(q_h \rho_h Cp_h\right)$ and m_c $\left(q_c \rho_c Cp_c\right)$ are the heat capacity rates in the hot-saline feed stream and cold feed stream, respectively.

Three simultaneous ordinary differential equations, Equations (25)–(27), involving the three variable functions H_m, $\gamma_{m,1}$ and $\gamma_{m,2}$ were solved iteratively along the membrane distillation module incorporating estimated convective heat-transfer coefficients $h_{h,1}$ and $h_{h,2}$ derived from Equations (23) and (24) by using the fourth-order Runge-Kutta method along the axial coordinate z in the flow direction. The 4th order Runge-Kutta method was chosen to minimize the trade-off between accuracy and computational efficiency to compute the temperature distributions of $T_{h,1}$, $T_{h,2}$ and T_c, from which the enhanced permeate flux and corresponding improvements were subsequently obtained and validated experimentally until achieving the specified convergence tolerance.

3.3. Assessment of Heat-Transfer Rate Enhancement

Double-pass modules were implemented within the open conduit of the hot saline feed stream in place of a single-pass configuration. Their implementation enhances effectively disturbing the thermal boundary layer and overcoming the temperature polarization effect, which significantly contributes to improved flow characteristics and heat transfer near the membrane surface. The augmented convective heat-transfer coefficients were evaluated

by comparing them to those in modules using single-pass modules and across various recycle ratio configurations, thereby increasing the temperature driving force across the membrane. Improved heat-transfer coefficients for the various recycle ratios were proposed through multiple linear regression correlations for the heat-transfer enhancement factor α^E [47] and expressed in terms of the correlated Nusselt number. These correlations of α^E were expressed in terms of the correlated Nusselt number by incorporating dimensionless groups into Buckingham's π theorem. The correlated Nusselt number was integrated into the heat-transfer enhancement factor, α^E, to increase the heat-transfer coefficient and reduce the temperature polarization effect, thereby increasing the temperature driving force across the membrane. A simplified relationship [48,49] between Nu^R (the correlated Nusselt number for the double-pass channel with various recycle ratios) and Nu^D (the Nusselt number for double-flow channel with internal recycle, $R = 0$) was established as follows:

$$Nu^R = \frac{h_h^R De_h^h}{k} = \alpha^E Nu^D = f(R, Re, Pr) \tag{28}$$

The correlated Nusselt number Nu^R is defined for the module of the recycling double-pass configuration, while the Nusselt number Nu^D is the double-pass module with internal recycle (recycle ratio equal to zero), for which the correlation equation was regressed as:

$$\alpha^E = \frac{Nu^R}{Nu^D} = k_1 (R)^{k_2} (Re)^{k_3} (Pr)^{k_4} \tag{29}$$

where R, Re and Pr represent the recycle ratio, Reynolds number, and Prandtl number, respectively, and h_h^R is defined as the improved heat-transfer coefficient of a double-pass channel with external recycle, and De_h^h is the heat-transfer equivalent diameter [50].

3.4. Power Consumption Increment by Operating Double-Pass Modules

Investigations into the design of recycling double-pass AGMD modules incorporating external recycle were conducted to improve permeate flux performance. However, this design inherently increases energy consumption due to higher frictional losses caused by intensified turbulence. An inevitable hydraulic consumption increment is expected and extra energy consumption required due to conducting double-pass modules. For simplicity to make a comparison, the power consumption estimation only considers the Fanning friction factor (f_F) [17] in both the hot and cold feed streams and ignores pump efficiency and true hydraulic losses caused by a joint, or a diversion or a bending of a tube in fittings with known length as follows:

$$\hat{H}_i = q_h \rho_h \ell w_{f,h} + q_c \rho_c \ell w_{f,c}, i = single\ pass,\ double\ pass \tag{30}$$

$$\ell w_{f,h} = \frac{2 f_{F,h} \overline{u}_h^2 L}{D_{h,h}}, \ell w_{f,c} = \frac{2 f_{F,c} \overline{u}_c^2 L}{D_{h,c}} \tag{31}$$

The hydraulic equivalent diameters De_h and De_c of modules were calculated with an operation double-pass module and a single-pass channel of both hot saline and cold feed streams, respectively. The Fanning friction factor can be estimated under Reynolds numbers within $87.8 \leq Re_h \leq 572.7$ for the recycling double-pass operations using a correlation based on the aspect ratio of the channel $\beta = D/W$ [51,52], which addressed the Fanning friction factor correlation to be applicable with the constricted flow area for both sawtooth and aligned roughness features in the laminar flow region.

$$f_{F,h} = \frac{C}{Re_h}, f_{F,c} = \frac{C}{Re_c} \tag{32}$$

$$C = 24\left(1 - 1.3553\beta + 1.9467\beta^2 - 1.7012\beta^3 + 0.9564\beta^4 - 0.2537\beta^5\right) \tag{33}$$

The percentage of the energy consumption increment I_P for the module with inserted carbon-fiber-filled channels was illustrated in comparison to the module using the single-pass module as

$$I_P = \frac{\hat{H}_{double} - \hat{H}_{single}}{\hat{H}_{single}} \times 100\% \quad (34)$$

where the subscripts of *double* and *single* represent the modules using double-pass channels and single-pass channels, respectively.

3.5. Three-Dimensional CFD Simulation of the Hot Saline Subchannel

To assess the hydrodynamic assumptions of the one-dimensional model (plug flow, uniform lateral distribution, and absence of stagnant regions), the velocity field in the hot saline feed subchannel was computed by three-dimensional computational fluid dynamics (CFD). Because the two subchannels have identical geometry and are traversed in series by the same volumetric flow rate, $Q = (1 + R)q_h$ (Figure 8a), one subchannel was simulated, and the mirror symmetry of the subchannel about the port center-plane ($W/2$) was used to halve the computational domain. The domain comprises a flow channel of 145 mm width, 210 mm length, and 2 mm height, bounded by the membrane and the acrylic plate, and the two semicircular distribution trenches of 12 mm diameter machined into the plate at both ends of the channel. The inlet and outlet ports (bore diameter 8.68 mm), located at the mid-width of the channel, open into the outer side of the trenches; they were represented by velocity-inlet and pressure-outlet patches on the outer quarter of the trench wall, with the same cross-sectional area as the bore and a uniform velocity directed along the port axis. The flow was treated as steady, incompressible and isothermal with the properties of the 3.5 wt% NaCl feed at 50 °C ($\rho = 1014$ kgm^{-3}, $\mu = 5.93 \times 10^{-4}$ Pas). The transmembrane permeation velocity (below 2×10^{-6} ms^{-1}) is more than four orders of magnitude smaller than the mean channel velocity and was neglected; i.e., the membrane was treated as an impermeable no-slip wall. The continuity and Navier–Stokes equations were solved with Green–Gauss gradients and implicit pseudo-time marching,

$$\nabla \cdot \mathrm{u} = 0, \rho(\mathrm{u} \bullet \nabla)\mathrm{u} = -\nabla \mathrm{P} + \mu \nabla^2 \mathrm{u} \quad (35)$$

No-slip conditions were imposed on the membrane and all plate walls, symmetry at the centre-plane, and zero gauge pressure at the outlet. The channel Reynolds number, $Re_h = \rho U_m D e_h^h / \mu$ with $U_m = Q/(Wd/2)$, ranges from 116 to 610 for $Q = 0.3 \sim 1.575$ L min^{-1}, which covers all combinations of q_h and R in the experiments (Table 2), so a laminar model was used. Because the port Reynolds number reaches $Re_h = 1254 \sim 6581$, the k − ω SST (shear stress transport) turbulence model [53] was applied at $Q = 0.3$ and 1.575 L min^{-1} as a sensitivity check. The block-structured hexahedral mesh had 12 cells across the channel height, 0.5 mm cells in the trenches, and lateral clustering around the port; three meshes with 7.6×10^4, 1.82×10^5 and 4.41×10^5 cells (half domain) were compared (Table 3). The local pressure gradient in the central part of the channel agrees with the Hele-Shaw flow relation [45] within 2% at $Re_h = 116$, which verifies the resolution across the 2-mm gap. The lateral flow distribution was characterized by the local flow rate per unit width, and by the maldistribution index averaged over the central part of the channel. A numerical residence-time distribution (RTD) was obtained by tracing massless tracer particles through the computed velocity field from about 3000 seeds distributed over the inlet patch, each weighted by the local inflow rate [54]. The residence times of the particles reaching the outlet give the flux-weighted exit-age distribution $E(\theta)$, with

$$\theta = t/\tau, \tau = V/Q \quad (36)$$

where V is the fluid volume of the subchannel including the trenches. Particles trapped in the no-slip layer at the walls (3–6% of the seeds) were excluded. Because molecular diffusion is neglected, the numerical RTD contains convective dispersion only and represents an upper bound of the spread. It was compared with plug flow (a pulse at $\theta = 1$) and with the RTD of an ideally distributed laminar slit flow, $E(\theta) = \left[3\theta^3\left(1 - \frac{2}{3\theta}\right)^{1/2}\right]^{-1}$ for $\theta \geq 2/3$, which accounts for the parabolic velocity profile across the gap alone.

Table 2. CFD results (laminar model, medium mesh) for the hot saline subchannel: maldistribution index, low-velocity area fraction, and characteristics of the numerical RTD.

Q (L min^{-1})	q_h (L min^{-1})/R	Re_h	Re_{port}	MI	A_{10} (%)	θ_{mean}	θ_{10}	θ_{50}	θ_{90}
0.3	0.3/0	116	1254	0.161	3.4	1.010	0.49	0.73	1.90
0.5	0.5/0	194	2089	0.181	3.4	0.992	0.50	0.69	1.72
0.7	0.7/0	271	2925	0.231	3.7	0.946	0.52	0.66	1.53
0.9	0.9/0	349	3761	0.275	3.3	0.978	0.52	0.66	1.75
1.125	0.9/0.25	436	4701	0.323	3.0	0.981	0.52	0.66	1.68
1.35	0.9/0.5	523	5641	0.369	2.8	0.985	0.52	0.68	1.74
1.575	0.9/0.75	610	6581	0.407	2.7	0.997	0.51	0.69	1.80
Ideal laminar slit	–	–	–	0	0	1	0.67	0.76	1.42

Table 3. Mesh independence, stationarity, and flow-model sensitivity of the CFD results.

Case (Q = 1.575 L min^{-1} Unless Stated)	Cells	MI	A_{10} (%)	θ_{mean}	θ_{50}
Laminar, coarse mesh	76,464	0.346	2.6	1.010	0.70
Laminar, medium mesh (reference)	182,016	0.407	2.7	0.997	0.69
Laminar, fine mesh	440,960	0.368	3.9	0.990	0.70
Laminar, medium mesh, +300 iterations	182,016	0.407	2.5	0.976	0.69
SST k − ω, medium mesh	182,016	0.171	3.9	1.003	0.72
SST k − ω, medium mesh, Q = 0.9 L min^{-1}	182,016	0.165	3.7	1.009	0.72
Laminar, medium mesh, Q = 0.9 L min^{-1}	182,016	0.275	3.3	0.978	0.66

4. Results and Discussions

4.1. Hydrodynamic Assessment of the Double-Pass Subchannel by CFD

Figure 10 shows the depth-averaged velocity magnitude, normalized by U_m, together with depth-averaged streamlines at the lowest ($Re_h = 116$), an intermediate ($Re_h = 349$) and the highest flow rate ($Re_h = 610$) through the subchannel. The feed enters the distribution trench as a jet, spreads along the trench and leaves it over the full width of the channel; no recirculation occurs in the membrane section, and downstream of $z \approx 50$ mm the streamlines are essentially parallel to the main flow direction. Low-velocity regions ($\overline{U} < 0.25\, U_m$, orange contours) are confined to thin layers along the side walls and to the edges of the trenches. The fraction of the membrane area with $\overline{U} < 0.1\, U_m$ remains between 2.7% and 3.7% over the whole range of operating conditions (Table 2). Hence, the module has no dead zones of practical significance, and practically the entire membrane area is swept by the feed.

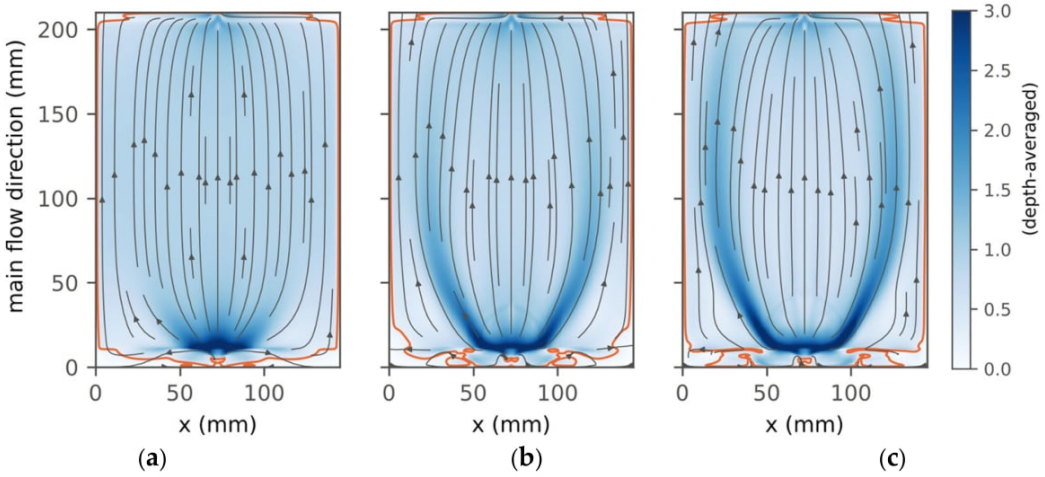


Figure 10. Depth-averaged velocity magnitude $\overline{U}/U_m$ and depth-averaged streamlines in the hot saline subchannel (laminar model; full width shown; flow from bottom to top). Orange contours: $\overline{U} = 0.25\,U_m$. (**a**) $Re_h = 116$ ($Q = 0.3$ L min^{-1}); (**b**) $Re_h = 349$ ($Q = 0.9$ L min^{-1}); (**c**) $Re_h = 610$ ($Q = 1.575$ L min^{-1}).

The lateral distribution of the flow, in contrast, depends on the flow rate (Figure 11). At $Re_h = 116$, the local flow per unit width is close to its mean across the width, apart from the boundary layers at the side walls. With increasing Re_h, the momentum of the inlet jet is carried along the trench, and two preferential streams leave the trench obliquely and travel along the channel at about 20–35 mm from the side walls, while the central part of the channel receives less flow. With the laminar model, the maldistribution index increases monotonically from 0.16 at $Re_h = 116$ to 0.41 at $Re_h = 610$ (Table 2). The lateral flow distribution was characterized by the local flow rate per unit width and by the maldistribution index (MI) averaged over the central part of the channel (50 mm ≤ z ≤ 160 mm). Since the flow rate through each subchannel is $(1 + R)q_h$, the recycle ratio acts in the same way: at $q_h = 0.9$ L min^{-1}, MI increases from 0.28 ($R = 0$) to 0.41 ($R = 0.75$). This trend, however, depends on the flow model.

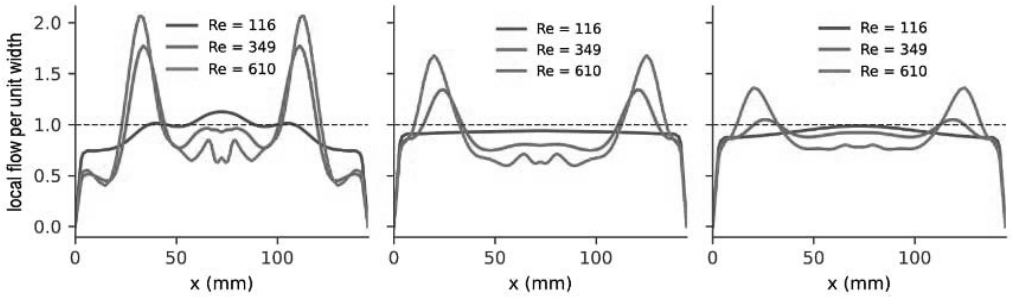


Figure 11. Lateral distribution of the local flow rate per unit width at three positions along the channel for $Re_h = 116$ (Blue Line), $Re_h = 349$ (Orange line) and $Re_h = 610$ (Green line).

The numerical RTDs (Figure 12a) confirm these observations. The mean dimensionless residence time θ_{mean} lies between 0.95 and 1.01 for all flow rates, i.e., the whole fluid volume, including the trenches, takes part in the flow, which excludes a significant stagnant volume. Compared with the ideally distributed laminar slit flow, for which the first tracer leaves at $\theta = 2/3$ and half of the flow has left at $\theta = 0.76$, the CFD distributions are shifted to earlier times ($\theta_{10} = 0.49 \sim 0.52$, $\theta_{50} = 0.66 \sim 0.73$), which reflects the faster preferential paths, and their tails ($\theta_{90} = 1.53 \sim 1.90$, compared with 1.42) reflect the slow fluid near the walls and in the trenches (θ_{10}, θ_{50}, θ_{90}: dimensionless times at which 10%, 50% and 90%

of the flow has left the subchannel). The RTD is thus far from plug flow; however, most of this deviation is caused by the parabolic velocity profile across the 2-mm gap, which is inherent in laminar channel flow and is already present in the ideal slit, whereas the additional broadening caused by the module geometry is moderate. With the SST model, which accounts for the turbulent mixing of the port jet ($Re_{port} = 3761 \sim 6581$ at these flow rates), MI is only 0.165 and 0.171 at $Q = 0.9$ and 1.575 L min^{-1} (Figure 12b), because the jet momentum is largely dissipated within the trench; the mean eddy viscosity falls below about 1% of the molecular viscosity downstream of z = 100 mm, so the channel flow itself remains laminar. The laminar results therefore represent an upper bound of the maldistribution, and the actual MI at high recycle ratios is expected to lie between the two estimates. In either case, the external recycle enhances the convective heat transfer without creating stagnant zones, but at the expense of a less uniform lateral distribution of the feed in the laminar limit.

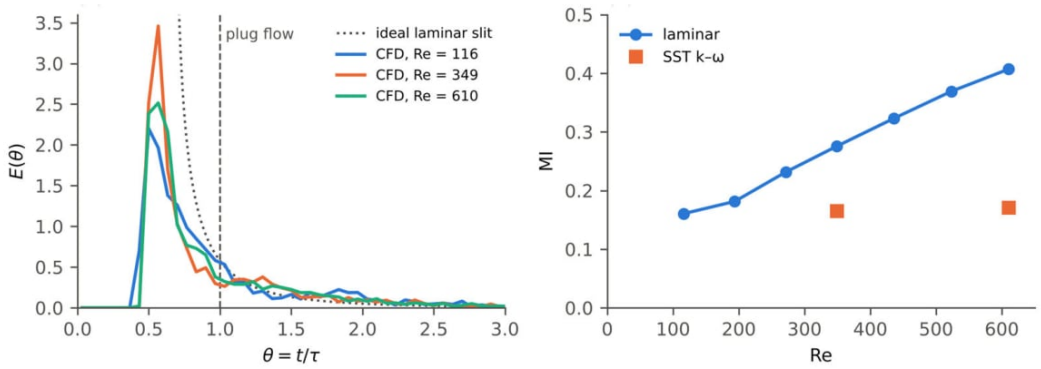


Figure 12. (**a**) Numerical residence-time distributions $E(\theta)$ of the hot saline subchannel compared with an ideally distributed laminar slit flow and with plug flow; (**b**) maldistribution index MI as a function of the channel Reynolds number (laminar and k − ω SST models).

These results bear directly on the assumptions of the one-dimensional model (Section 3.2). Because the model is formulated with cross-sectionally averaged temperatures and length-averaged heat-transfer coefficients regressed from measured permeate fluxes (Equations (28), (29), (37) and (38)), it does not require a flat velocity profile across the gap; the relevant hydrodynamic assumptions are the absence of stagnant zones and a uniform lateral distribution. The first is supported by the CFD at all operating conditions. The second holds well at low flow rates and becomes increasingly approximate at the highest flow rates and recycle ratios. Using the second-order sensitivity estimate of Section 3.2 (less than 0.5% change in the predicted flux for a ±20% lateral imbalance), the computed MI values correspond to flux deviations of about 0.3–2.1%, which is consistent with the small over-prediction of the permeate flux at the higher flow rates in Table 4. In addition, the regressed enhancement factor α^E implicitly accounts for the actual flow distribution in the module. From a design viewpoint, a single central port is adequate at low and moderate flow rates, whereas operation at high recycle ratios would benefit from a distributor with several ports or a perforated baffle in the trench to restore lateral uniformity.

The numerical uncertainty was assessed as summarized in Table 3. At the highest flow rate, where the jet-driven flow in the trench is most sensitive to the resolution, θ_{mean} and θ_{50} differ by less than 2% between the medium and the fine mesh; stagnant regions were identified by A_{10}, the fraction of the membrane area at which the depth-averaged velocity is below 10% of U_m. A_{10} by 1.2 percentage points and MI by 10% (coarse mesh: MI = 0.346); the MI values at the highest Reynolds numbers are therefore uncertain by

about ±10%, which does not affect the conclusions. The medium mesh was used for all results. Continuing the medium-mesh solution at the highest flow rate for another 300 iterations changed MI by 0.1% and θ_{50} by 0.3%, confirming that the solution is stationary.

4.2. Estimation of Convective Heat-Transfer Coefficients in the Correlated Nusselt Number

The estimated convective heat-transfer coefficients, expressed in terms of the correlated Nusselt number for recycling double-pass channels with external recycle, were calculated using the correlation given in Equation (28) and compared with those of a double-pass module with internal recycle ($R = 0$). The heat-transfer enhancement factor, α^E, defined in Equation (29), was obtained through regression analysis by solving the resultant normal equations for the least-squares parameters to obtain the correlated equation and the squared correlation coefficient within 0.94~0.96. The heat transfer enhancement factor, α^E, was expressed using Equation (29), in conjunction with Equations (35) and (36), as illustrated in Figure 13, and the heat-transfer coefficients, expressed in terms of the correlated Nusselt number, were determined using a theoretical model and compared with a double-pass module with internal recycle. It is concluded from Figure 13 that these corrected Nusselt numbers are more significant trendy the modules with implementing the double-pass modules with internal ($R = 0$) or external recycle ($R \neq 0$) due to the strengthened convective heat-transfer rate.

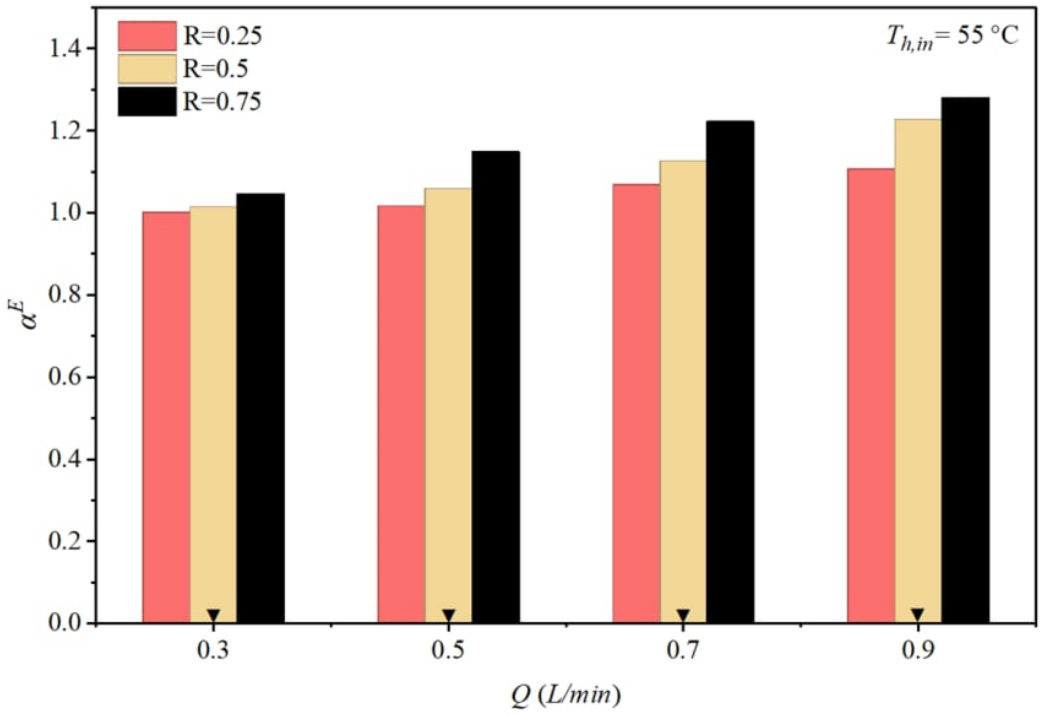


Figure 13. Comparisons of correlated Nusselt numbers for recycling double-pass configurations with various recycle ratios.

The heat-transfer coefficients, expressed in terms of the correlated Nusselt number, were determined using a theoretical model in Equation (36) with external recycle ($R \neq 0$) and compared to a module with internal ($R = 0$). The results align linearly with the experimental data, as shown in Figure 14. The correlation expression of Nusselt numbers is applicable for double-pass modules with external recycle. Another aspect to consider is the improved device performance to disrupt the thermal boundary layer and increase permeate flux.

$$Nu_D = 1.97(Re)^{0.12}(Pr)^{0.21} \quad (37)$$

$$Nu^R = 0.41(R)^{0.02}\ (Re)^{0.30}(Pr)^{0.66} \quad (38)$$

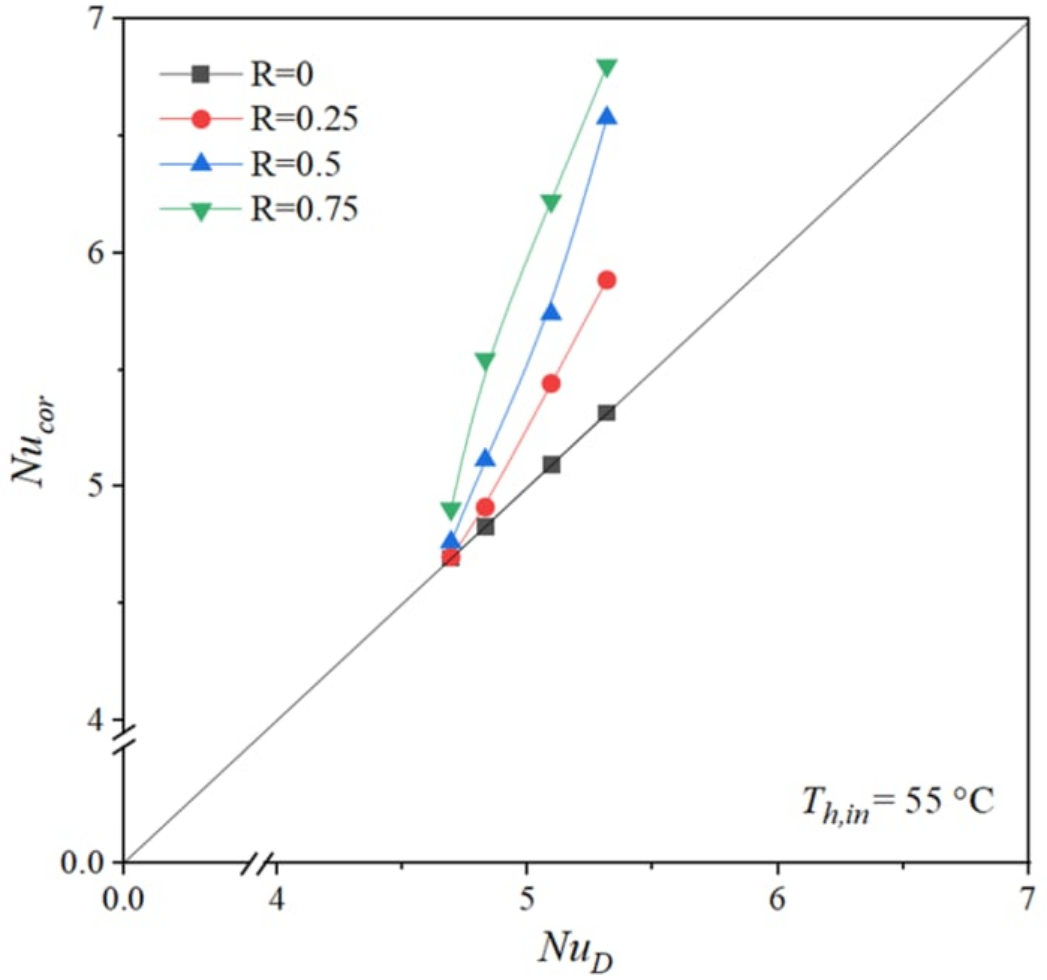


Figure 14. Comparisons between correlated and experimental Nusselt numbers for double-pass modules under various recycle ratios.

4.3. Lessening Temperature Polarization Effect by Operating Double-Pass Modules

Temperature distributions for both the hot saline and cold feed streams were determined by solving three simultaneous ordinary differential equations, Equations (25)–(27), using the fourth-order Runge–Kutta method along the module's flow channel, which quantify the enhanced permeate flux and reduced temperature polarization effect resulting from increased convective heat-transfer coefficients due to the double-pass operations. This enhancement, brought about by operating double-pass modules, reduces the thermal boundary layer thickness and consequently leads to a larger temperature polarization coefficient. However, the temperature gradients across the membrane surfaces are consistently larger in double-pass modules compared to those in single-pass modules. As a result, higher permeate flux is achieved in the double-pass modules due to the stronger temperature driving force. Theoretical predictions of the temperature polarization coefficient, $\gamma_{m,1}$ and $\gamma_{m,2}$, were obtained from Equations (23) and (24), which illustrate the temperature polarization coefficient of both subchannels in Figure 15a,b with the inlet hot saline temperature and recycle ratio used as parameters for double-pass operations.

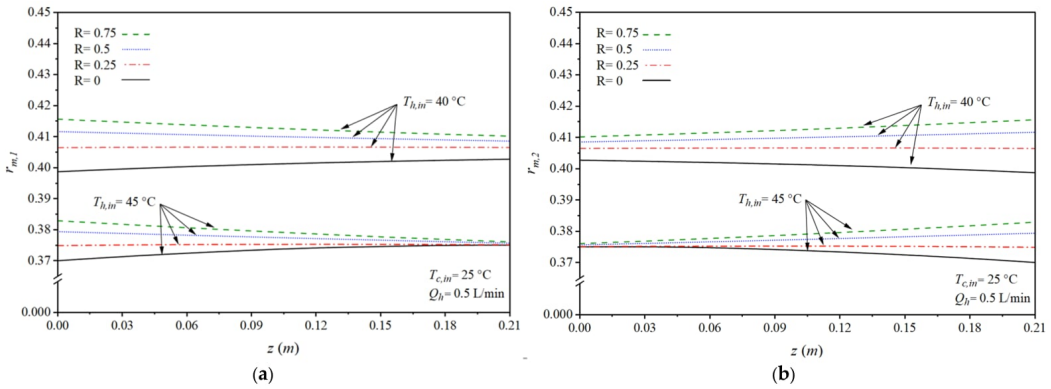


Figure 15. Effects of inlet hot saline feed temperature and various ratios on the temperature polarization coefficient. (**a**) Left-hand-side channel; (**b**) Right-hand-side channel.

Equation (1) linearizes the vapor-pressure difference between T_1 and T_3, i.e., across the membrane and the air gap. For the present operating conditions $\gamma_m = 0.37 \sim 0.42$ shown in Figure 15, so that $(T_1 - T_3) \leq 12.6$ K, which lies within the $\Delta T < 15$ K limit of this approximation [1]. Because $P^{sat}(T)$ is convex, the tangent at T_m slightly underestimates the exact difference; comparison with the exact Antoine difference gives deviations of -0.1% to -1.2% (-0.7% to -2.0% for the Clausius–Clapeyron form) over the whole operating range, well below the $\pm 5\%$ experimental reproducibility. The resulting quantitative checks are collected in a new Appendix A (Table A1). As the recycle ratio increases but the inlet hot saline temperature decreases, the associated rise in vapor pressure leads to higher permeate flux through the membrane due to the enlarged temperature difference across the membrane surfaces and the corresponding increase in the temperature polarization coefficient. Furthermore, the temperature polarization effect is more pronounced in the first channel (left-hand-side) of the module compared to the latter channel (right-hand-side). Restated, the higher inlet saline temperature produces a higher permeate flux, resulting in a lower temperature difference across the membrane surfaces. As the salinity in the hot saline feed stream is increased along the channel due to the loss of pure water that reduces water activity coefficient of the hot saline stream, therefore, the saturation pressure of the hot saline stream is reduced that also reduces the pressure gradient across the membrane. The decreasing heat transfer rate and permeate along the channel in the left-hand-side channel is thus expected.

4.4. Permeate Flux Improvement by Implementing Double-Pass Modules

The accuracy deviation of the theoretical predictions of permeate fluxes with respect to experimental results for all measurements of recycling double-pass operations as illustrations was calculated using the following definition as follows [55]:

$$E\ (\%) = \frac{1}{N_{exp}} \sum_{j=1}^{N_{exp}} \frac{\left| N''_{theo,j} - N''_{exp,j} \right|}{N''_{exp,j}} \tag{39}$$

Moffat [55] calculated the experimental uncertainty for each individual measurement from the experimental runs as follows:

$$S_{N''_{exp,j}} = \left\{ \sum_{i=1}^{N_{exp}} \frac{\left(N''_{exp,j} - \overline{N''_{exp,j}} \right)^2}{N_{exp} - 1} \right\}^{1/2} \tag{40}$$

The mean value of the resulting uncertainty of the experimental measurements was defined by

$$S_{\overline{N''_{exp,j}}} = \frac{S_{N''_{exp,j}}}{\sqrt{N_{exp}}} \quad (41)$$

where N_{exp}, $N''_{theo,j}$, $N''_{exp,j}$ and $\overline{N''_{exp,j}}$ are the number of experimental runs, theoretical predictions, experimental results of permeate fluxes, and the mean value of experimental results of permeate fluxes, respectively. The deviation and uncertainty of the experimental measurements are well minimized within $2.2 \times 10^{-3} \leq E \leq 9.96 \times 10^{-2}$ and $5.24 \times 10^{-3} \leq S_{\overline{J_{exp}}} \leq 8.85 \times 10^{-3}$, respectively. It is seen from Table 4 that good agreement was observed between the theoretical predictions and experimental results for permeate flux, supporting strong evidence for the proposed design's efficacy. The experimental setup comprised two parallel-plate channels divided by a total hydrophobic composite membrane area of 0.21 m length and 0.29 m width. The insertion of straight carbon-fiber spacers near the membrane surface in the air-gap channel obstructed approximately 13% of the effective hydrophobic membrane surface area, which was counted as the effective permeate flux area in the calculation procedure due to blocking permeate flux throughout the membrane.

The results also show that the module with using double-pass modules enhances more heat-transfer rate significantly than those in the modules with using single-pass modules. This is because the convective heat-transfer coefficient is strengthened in double-pass modules, as depicted in Figure 16. Moreover, this study graphically compares theoretical predictions of permeate flux for recycling double-pass modules with various recycle ratios. Improved device performance was observed in modules with a larger recycle ratio, achieving higher permeate flux, as illustrated in Figure 17a,b for $R = 0.25$ and $R = 0.5$, respectively. Permeate flux was found to increase with higher hot saline feed flow rates and volumetric flow rates. The agreement between theoretical predictions and experimental data is reasonably consistent, as demonstrated in Figure 17a,b. This indicates that the operation with the larger recycle ratio yields higher permeate flux than the operation with the smaller recycle ratio due to better suppression of the boundary layer effects.

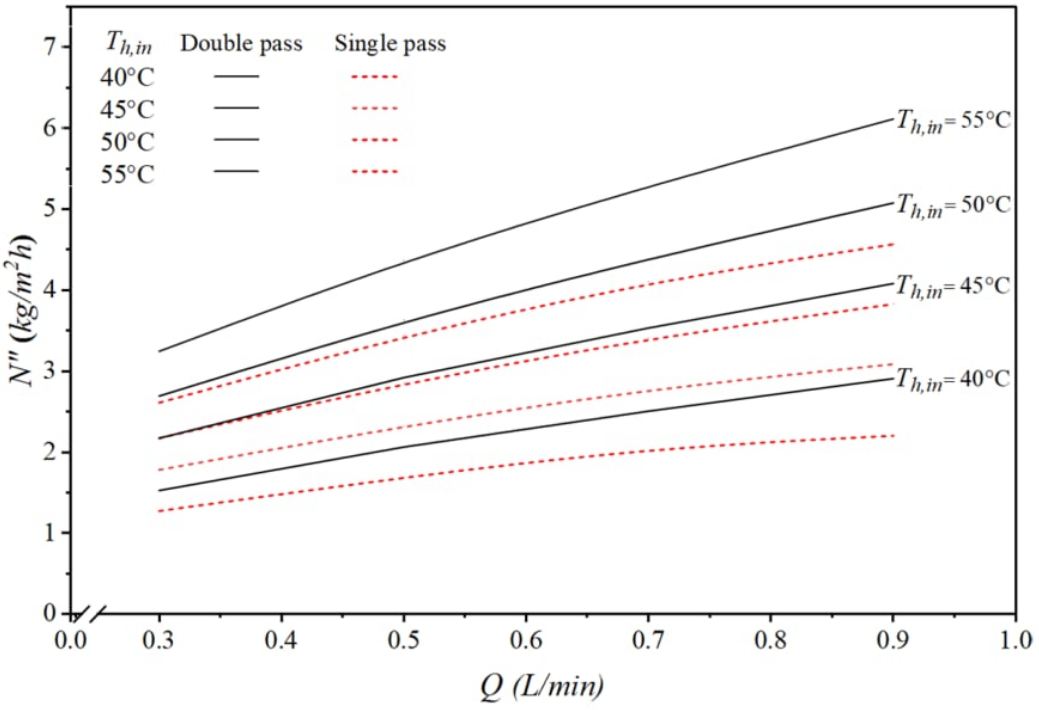


Figure 16. Effects of single- and double-pass ($R = 0.25$) configurations on permeate flux.

Table 4. The accuracy deviation between theoretical predictions N''_{theo} and experimental results N''_{exp} of permeate fluxes.

$T_{h,in}$ (°C)	q_h (L/min)	Recycling Double-Pass Module					
		$R = 0.25$			$R = 0.5$		
		N''_{exp} (kg m^{-2} h^{-1})	N''_{theo} (kg m^{-2} h^{-1})	E (%)	N''_{exp} (kg m^{-2} h^{-1})	N''_{theo} (kg m^{-2} h^{-1})	E (%)
40	0.3	1.68	1.60	5.31	1.79	1.66	8.07
	0.5	2.03	2.18	7.00	2.30	2.38	3.48
	0.7	2.79	2.74	1.92	2.98	3.03	1.71
	0.9	3.04	3.25	6.44	3.57	3.64	1.77
45	0.3	2.29	2.23	2.87	2.49	2.32	7.46
	0.5	3.16	3.07	3.05	3.09	3.36	7.98
	0.7	3.60	3.84	6.13	3.80	4.26	9.96
	0.9	4.28	4.55	5.87	4.69	5.10	8.05
50	0.3	2.91	2.75	5.98	3.03	2.87	5.66
	0.5	3.54	3.81	6.98	3.93	4.15	5.24
	0.7	4.33	4.76	8.96	4.79	5.26	8.91
	0.9	5.15	5.64	8.62	5.77	6.29	8.27
55	0.3	3.27	3.29	0.50	3.46	3.45	0.22
	0.5	4.16	4.58	9.16	4.65	4.96	6.38
	0.7	5.48	5.72	4.23	5.88	6.31	6.76
	0.9	6.23	6.76	7.79	6.85	7.56	9.37

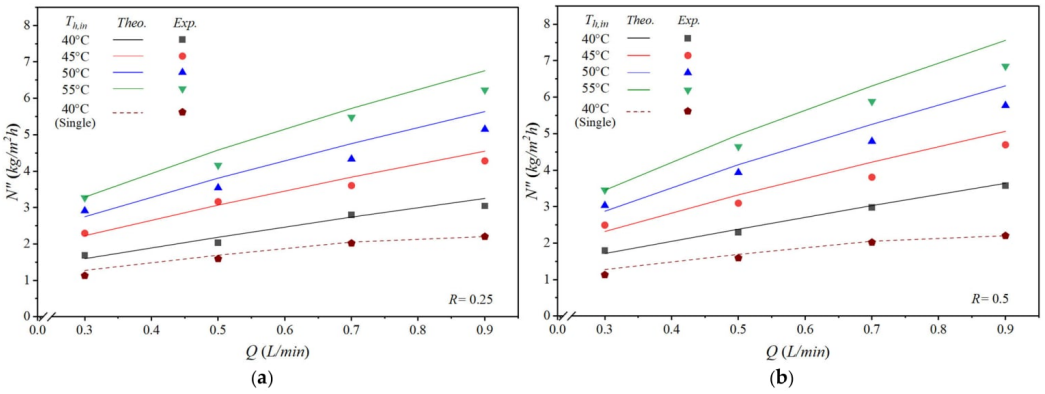


Figure 17. Comparisons of theoretical and experimental permeate fluxes for recycling double-pass AGMD modules under various recycle ratios. (**a**) $R = 0.25$; (**b**) $R = 0.5$.

It is noteworthy that a higher permeate flux was achieved at elevated inlet hot feed temperatures, with the order of permeate flux magnitude following: 55 °C > 50 °C > 45 °C > 40 °C, attributed to the increased temperature driving force, which generated a larger temperature gradient across the membrane, resulting in greater permeate flux. Furthermore, the influence of recycle ratio on the permeate flux for better comparison was presented in Figure 18. This effect is particularly pronounced with a larger recycle ratio under the same working dimension, mitigating the thermal boundary layer and leading to the permeate flux improvement.

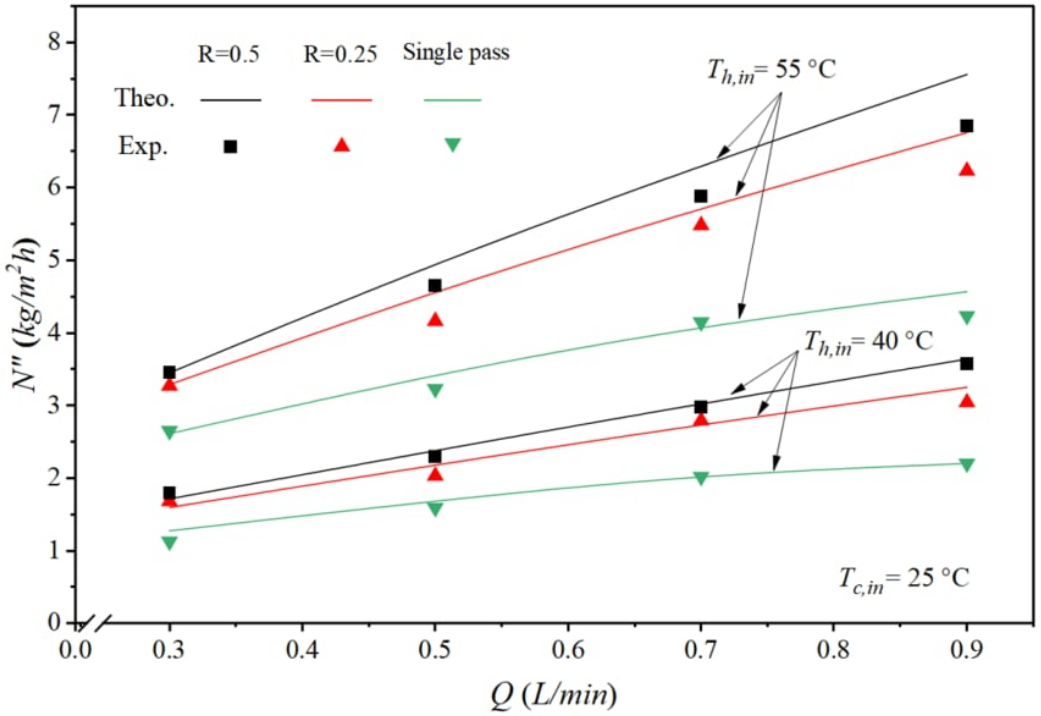


Figure 18. Comparison of recycle ratio and permeate flux for recycling double-pass AGMD modules.

As expected, modules incorporating double-pass modules exhibited significant improvements in permeate flux compared to those utilizing single-pass modules. The relative permeate flux improvements (I_N) were quantified by calculating the percentage increase between the permeate flux of the module with a double-pass module ($R = 0$) and that of the module using a single-pass channel, as shown below.

$$I_N = \frac{N''_{double} - N''_{single}}{N''_{single}} \times 100\% \quad (42)$$

where the subscripts *double* and *single* represent the module channels with operating double- and single-pass channels, respectively.

Theoretical predictions of permeate flux improvements (I_N) for membrane distillation modules incorporating single- and double-pass operations are summarized in Table 5, with inlet hot saline feed temperature and feed flow rate as parameters. The results show that I_N increases with both higher inlet hot feed temperatures and hot feed flow rates. Analysis indicates that implementing a double-pass module with internal recycle ($R = 0$) significantly enhances permeate flux compared to the single-pass configuration, primarily by mitigating the temperature polarization effect. Device performance for the double-pass module with internal recycle ($R = 0$), as confirmed in Table 5. Notably, the double-pass module achieved a relative permeate flux increase of up to 33.91% at an inlet hot feed temperature of 55 °C and a feed flow rate of 0.9 L/min compared to the single-pass module. The double-pass AGMD module demonstrates a significant enhancement in permeate flux, confirming its technical viability for device performance improvement in double-pass modules.

The present work extends the previous study of inserting cross-diagonal carbon-fiber spacers [56] to recycling double-pass operations. The graphical representation for comparisons with theoretical predictions and experimental results of the permeate flux obtained in the present study using cross-diagonal carbon-fiber spacers [56] demonstrates why the present configurations of double-pass AGMD modules with external recycle are preferred and are presented in Figure 19 under various inlet hot saline temperatures.

Table 5. Effects of double-pass operations on permeate flux improvements I_N.

$T_{h,in}$ (°C)	q_h (L/min)	Single Pass	Double Pass ($R = 0$)	
		N''_{single} ($kg\ m^{-2}\ h^{-1}$)	N''_{double} ($kg\ m^{-2}\ h^{-1}$)	I_N (%)
40	0.3	1.27	1.53	19.92
	0.5	1.69	2.06	21.99
	0.7	2.05	2.51	22.19
	0.9	2.20	2.91	32.08
45	0.3	1.78	2.17	21.84
	0.5	2.32	2.92	25.56
	0.7	2.78	3.53	27.12
	0.9	3.08	4.08	32.33
50	0.3	2.17	2.69	23.89
	0.5	2.85	3.63	27.07
	0.7	3.41	4.39	28.89
	0.9	3.83	5.08	32.61
55	0.3	2.61	3.24	24.28
	0.5	3.44	4.37	27.10
	0.7	4.10	5.29	28.95
	0.9	4.57	6.11	33.91

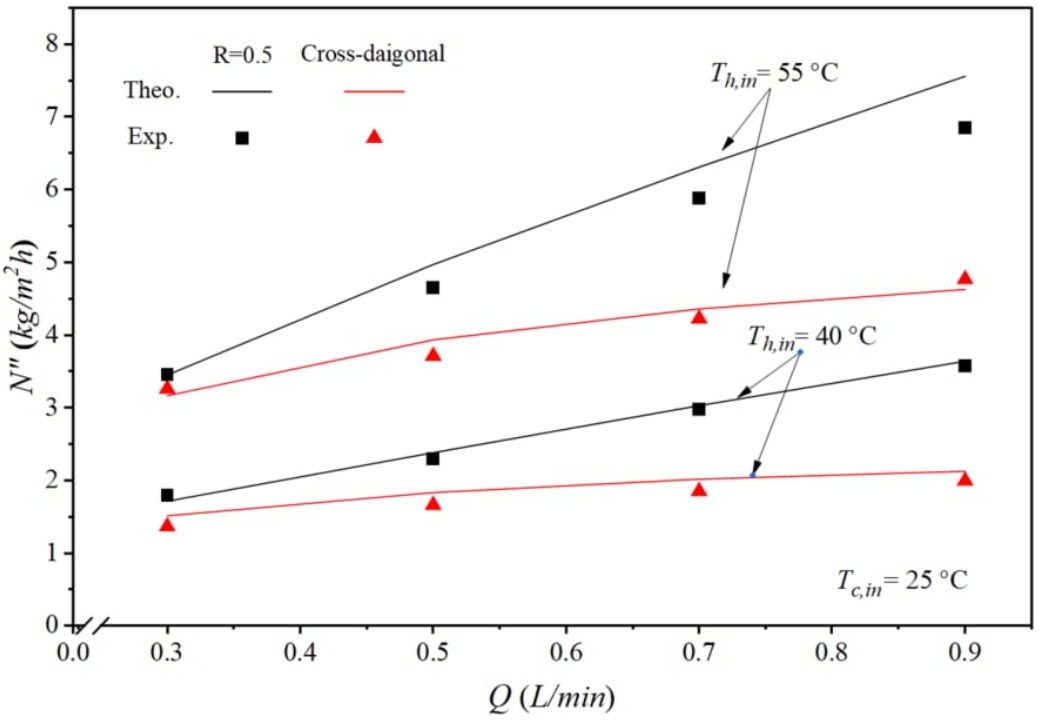


Figure 19. Comparison of theoretical predictions and experimental results of the permeate flux.

Moreover, the interpretation of mechanistic analysis on the permeate flux improvement in the double-pass operation demonstrates the thermal resistance reduction due to mitigating the thermal boundary layer with a smaller thermal resistance. The thermal

resistance (or convection resistance) was defined by $R_{conv} = \frac{1}{h_h A}$, and the results show that the thermal resistances decrease with both the inlet hot saline temperatures and the hot saline feed flow rates, as shown in Table 6.

Table 6. Thermal resistances of modules for both single- and double-flow operations.

$T_{h,i}$ (°C)	q_h (L/min)	Thermal Resistances × 10^2 (K/W)				
		Single Pass	Double Pass $R = 0$	Recycling Double Pass		
				$R = 0.25$	$R = 0.5$	$R = 0.75$
40	0.3	22.35	2.22	2.22	2.16	2.12
	0.5	15.51	2.17	2.09	2.03	1.99
	0.7	11.43	2.14	2.00	1.95	1.90
	0.9	10.42	2.11	1.94	1.88	1.83
45	0.3	18.33	2.21	2.23	2.17	2.13
	0.5	14.98	2.16	2.10	2.04	2.00
	0.7	12.71	2.12	2.01	1.96	1.91
	0.9	10.24	2.10	1.95	1.89	1.85
50	0.3	19.37	2.19	2.23	2.18	2.14
	0.5	15.36	2.14	2.11	2.05	2.01
	0.7	13.92	2.11	2.02	1.97	1.92
	0.9	12.05	2.10	1.96	1.90	1.86
55	0.3	18.47	2.18	2.24	2.18	2.14
	0.5	15.50	2.13	2.11	2.06	2.02
	0.7	13.09	2.10	2.03	1.98	1.93
	0.9	12.26	2.08	1.97	1.91	1.87

4.5. Further Permeate Flux Enhancement

Recycling double-pass configurations were employed in AGMD membrane distillation modules, tested under various recycle ratios. The further permeate flux enhancement (E_R) was calculated based on the performance of recycling double-pass modules with external recycle ($R \neq 0$) relative to double-pass modules with internal recycle ($R = 0$) under identical conditions. The enhancement was determined using the following relationship:

$$E_R(\%) = \frac{N''_R - N''_{R=0}}{N''_{R=0}} \times 100 = \left[\frac{\left(N''_R - N''_{single}\right) - \left(N''_{R=0} - N''_{single}\right)}{N''_{single}}\right]\left(\frac{N''_{single}}{N''_{R=0}}\right) \times 100 = \left(I_N^R - I_N^{R=0}\right)/\left(1 + I_N^{R=0}\right) \times 100 \quad (43)$$

where $N''_{R=0}$ and N''_R represent the permeate fluxes in the modules embedded with double-pass modules of $R = 0$ and recycling double-pass modules with various ratios ($R \neq 0$), respectively. Likewise, $I_N^{R=0}$ and I_N^R denote the permeate flux improvements in the corresponding modules. The percentage improvements in permeate flux (I_N) and further permeate flux enhancements (E_R) for recycling double-pass modules with external recycle are summarized in Table 7 using inlet hot saline temperature, volumetric flow rate, and recycle ratio as variables. Specifically, the relative improvement in permeate flux reached up to 82.51% for recycling double-pass modules with $R = 0.75$, when compared to the single-pass module. As demonstrated, the implementation of double-pass modules in the hot saline feed stream led to noticeable augmentation in convective heat-transfer coefficients, resulting in increased permeate vapor transport across the membrane. This further permeate flux

enhancement was calculated based on comparison with the double-pass configuration with $R = 0$. The results indicate that further permeate flux enhancements increase with higher inlet saline temperatures and hot saline feed flow rates. As an illustration, the further permeate flux enhancement of recycling double-pass operation with recycle ratio $R = 0.75$ was calculated at $T_{h,in} = 55$ °C and $Q = 0.9$ L/min, and then the further permeate flux enhancement of 35.77% was achieved with the use of results in Tables 5 and 7 as follows:

$$E_R(\%) = \left(I_N^R - I_N^{R=0}\right)/\left(1 + I_N^{R=0}\right) \times 100 = (0.8181 - 0.3391)/(1 + 0.3391) \times 100 = 35.77 \quad (44)$$

Table 7. Theoretical predictions of permeate flux improvements and further permeate flux enhancement in the double-pass module with external recycle.

$T_{h,in}$ (°C)	Q (L/min)	Double-Pass Module with External Recycle					
		$R = 0.25$		$R = 0.5$		$R = 0.75$	
		I_N (%)	E_R (%)	I_N (%)	E_R (%)	I_N (%)	E_R (%)
40	0.3	25.36	4.54	30.43	8.77	41.06	17.63
	0.5	29.17	5.88	40.79	15.41	51.17	23.91
	0.7	33.49	9.24	47.65	20.83	60.91	31.68
	0.9	47.64	11.77	65.32	25.16	82.48	38.15
45	0.3	24.97	2.57	30.03	6.73	38.94	14.04
	0.5	31.91	5.06	44.53	15.11	55.07	23.50
	0.7	38.03	8.58	53.29	20.59	66.61	31.07
	0.9	47.39	11.38	65.45	25.03	82.51	37.92
50	0.3	26.39	2.02	31.92	6.48	40.16	13.13
	0.5	33.40	4.98	45.45	14.46	55.82	22.62
	0.7	39.65	8.35	54.33	19.73	67.51	29.96
	0.9	47.25	11.04	64.37	23.95	81.33	36.74
55	0.3	25.92	1.32	32.13	6.32	39.66	12.37
	0.5	33.22	4.81	44.34	13.57	54.91	21.88
	0.7	39.50	8.18	53.80	19.27	66.36	29.01
	0.9	47.99	10.52	65.54	23.62	81.81	35.77

4.6. Energy Consumption Increment

The ratio of permeate flux improvement to energy consumption increment, denoted as I_N/I_P, was used to examine the technical feasibility of implementing double-pass modules from an economic evaluation, which serves as an indicator of technical feasibility by quantifying optimal operating conditions for achieving enhanced permeate flux with reasonable energy costs. The results of I_N/I_P demonstrate that an increase in the percentage of the permeate flux improvement can effectively offset the rise in the percentage of the power consumption increment based on comparisons with he single-pass module and double-pass configuration with $R = 0$, as shown in Figure 20a,b, respectively. As shown in Figure 20a, double-pass modules can increase permeate flux more effectively at higher inlet hot saline temperatures given the associated increment in energy consumption. The relative percentage increase in permeate flux improvement exceeds the percentage increase in energy consumption when implementing double-pass modules with $R = 0$. In addition, the larger the value of I_N/I_P is obtained under the higher recycle ratio, the higher permeate

flux improvement is achieved, as seen in Figure 20b for the further estimation of I_N/I_P based on comparison with the double-pass configuration with $R = 0$. This is particularly evident in modules with recycling double-pass modules under various recycle ratios, which outperform single-pass modules as well as the double-pass configuration ($R = 0$) in terms of energy efficiency and overall device performance. The results show that I_N/I_P increases with the hot saline feed flow rate, the inlet hot saline temperature, and the recycle ratio, as presented in Figure 20b, which is consistent with the achieved economic feasibility by implementing recycling double-pass modules. As expected, recycling double-pass modules exhibited better performance than those in double-pass modules with internal recycle ($R = 0$). In other words, recycling double-pass modules offer greater potential for efficient permeate flux improvement compared to that of using single-pass modules and double-pass modules with internal recycle ($R = 0$), aligning better with economic and operational considerations.

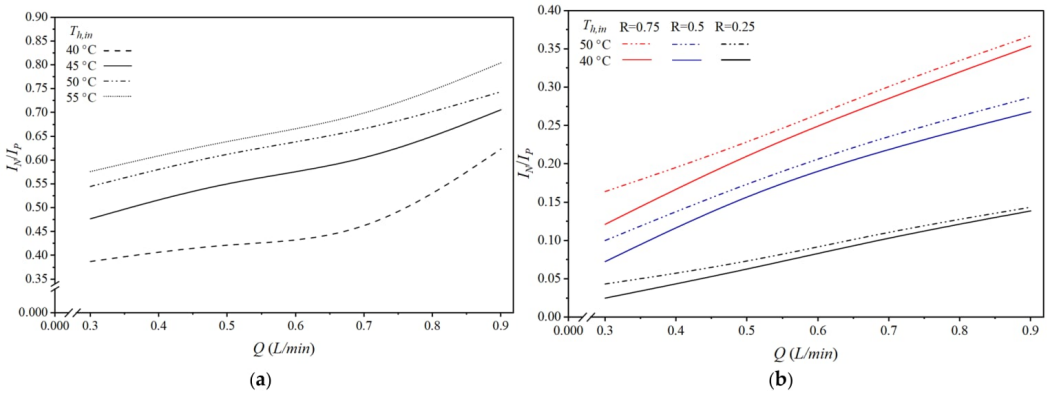


Figure 20. Comparisons of I_N/I_P with implementing double-pass configurations. (**a**) Double-pass modules vs. single-pass modules; (**b**) Double-pass modules with recycle ratios vs. double-pass modules with $R = 0$.

5. Conclusions

The theoretical predictions of permeate flux were simulated and validated by experimental results under various hot saline feed flow rates, inlet hot feed temperatures, recycle ratios, and single- and double-pass configurations. An assessment of the flow configurations for implementing recycling AGMD double-pass modules was conducted to determine the permeate flux improvement that balances the desirable increment of the convective heat-transfer coefficient and the undesirable increment of hydraulic power consumption. Overall, the implementation of the double-pass module exhibits significant potential for substantially augmenting permeate flux in the recycling AGMD module due to mitigating the temperature polarization effect. Thorough comparisons of permeate flux improvement through the employment of AGMD double-pass modules with external recycle in the hot saline feed stream lead to the following conclusions:

1. Implementing a double-pass module with internal recycle ($R = 0$) improves the permeate flux with a maximum increase of 33.91% obtained for the module with an internal-recycle configuration relative to the single-pass module.
2. Operating a recycling double-pass module with external recycle at $R = 0.75$ achieves a relative improvement in permeate flux of up to 82.51% and a further permeate flux enhancement of 38.15% as compared to a double-pass module with internal recycle ($R = 0$).
3. The results indicate that double-pass operations with internal ($R = 0$) or external ($R \neq 0$) recycle in AGMD modules achieve improved permeate flux as compared to

single-pass operations due to enhanced convective heat-transfer coefficients. Moreover, the larger the value of I_N/I_P is obtained in recycling double-pass modules with the higher recycle ratio, the higher permeate flux improvement is achieved for the further comparison of I_N/I_P with respect to the double-pass configuration with $R = 0$.

4. Three-dimensional CFD simulations of the feed subchannel ($Re_h = 116 \sim 610$) showed that the distribution trenches feed the whole membrane width without dead zones ($A_{10} < 4\%$, $\theta_{mean} = 0.95 \sim 1.01$), whereas the lateral maldistribution index lies between 0.16 and 0.41; the upper value is obtained with the laminar model at the highest recycle-enhanced flow rate, for which the k − ω SST model, accounting for the turbulent port jet, gives 0.17. The plug-flow description of the model is therefore well founded at low flow rates and remains a reasonable approximation (estimated flux error of at most about 2%) at the highest recycle ratios, where a multi-port distributor would improve the flow uniformity.

The regressed Nusselt number correlations derived from the theoretical model offer practical insights for designing and operating more efficient double-pass AGMD modules, especially for the double-pass modules with the larger recycle ratios. Additionally, this work emphasizes the potential of exploring internal recycle and external recycle for optimizing AGMD operations by validating both the technical feasibility and device performance benefits of such designs. The approach presented herein can also be extended to other membrane separation processes for future investigations of both technical and economic considerations.

Limitations and future work. The hydrodynamic assessment is based on steady, isothermal CFD simulations with an idealized representation of the port openings, and the numerical RTD neglects molecular diffusion. Experimental tracer-response measurements would provide a direct validation of the numerical RTD and are planned, together with tests with real seawater and long-term operation; a multi-port or perforated distributor will be examined for operation at high recycle ratios.

Author Contributions: Conceptualization and Writing—original draft, C.-D.H.; Data curation, J.-J.L.; Writing—review and editing, J.W.L.; Validation, Y.-C.Z. All authors have read and agreed to the published version of the manuscript.

Funding: The authors wish to thank the National Science and Technology Council (NSTC) of the Republic of China (Taiwan) for the financial support (grant number NSTC 115-2221-E-032-037).

Institutional Review Board Statement: Not applicable.

Informed Consent Statement: Not applicable.

Data Availability Statement: The original contributions presented in this study are included in the article. Further inquiries can be directed to the corresponding author.

Conflicts of Interest: The authors declare no conflict of interest.

List of Symbols

A	Cross-sectional area of flow channel (m^2)
a_w	Water activity in NaCl solution
C	Friction losses coefficient
C_P	Heat capacity (J kg^{-1} K^{-1})
c_a	Mass transfer coefficient of air gap ($kg \cdot m^{-2} \cdot Pa^{-1} \cdot h^{-1}$)
c_k	Membrane coefficient based on the Knudsen diffusion model (mol $m^{-2}Pa^{-1}s^{-1}$)
c_M	Membrane coefficient based on the molecular diffusion model (mol $m^{-2}Pa^{-1}s^{-1}$)
c_m	Membrane permeation coefficient (mol $m^{-2}Pa^{-1}s^{-1}$)
$C_{P,j}$	Heat capacity (J kg^{-1} K^{-1}), $j = 1, 2$

c_T	Overall mass transfer coefficient (kg m^{-2} Pa^{-1} h^{-1})
d	Channel height (m)
d_p	The nominal pore diameter (m)
D_m	Diffusion coefficient of air and vapor in the membrane (m^{2}s^{-1})
De_j	Hydraulic equivalent diameter of channel (m), $j = h, c$
De_h^h	Heat-transfer equivalent diameter of channel (m)
E	Accuracy deviation of experimental results from the theoretical predictions
E_R	Further permeate flux enhancement
$f_{F,c}$	Fanning friction factor for cold feed stream
$f_{F,h}$	Fanning friction factor for hot saline feed stream
g	Gravitational acceleration (ms^{-2})
H_c	Overall heat transfer coefficient of cold fluid (W m^{-2} K^{-1})
$\hat{H}_i$	Hydraulic dissipate energy (W), $i = h, c$
H_m	Thermal convection coefficient of membrane (W m^{-2} K^{-1})
h_c	Convection coefficient of cold fluid (W m^{-2} K^{-1})
h_f	Convection coefficient of condensation film (W m^{-2} K^{-1})
h_h	Convection coefficient of hot fluid (W m^{-2} K^{-1})
h_h^R	Improved heat-transfer coefficient of double-pass module (W m^{-2}K^{-1})
I_N	Permeate flux relative factor
I_p	Power consumption relative index
Kn	Knudsen number
k_a	Thermal conductivity coefficient of air gap (W m^{-1} K^{-1})
k_f	Thermal conductivity coefficient of condensate film (W m^{-1} K^{-1})
k_i	Regression constants, $i = 1, 2, 3, 4$
k_m	Average thermal conductivity coefficient of membrane (W m^{-1} K^{-1})
k_p	Average thermal conductivity coefficient of the cooling plate (W m^{-1} K^{-1})
L	Channel length (m)
$L_{e,h}$	The hydrodynamic entrance length (m)
$L_{e,t}$	The thermal entrance length (m)
$\ell w_{f,j}$	Friction loss (J kg^{-1}), $j = h, c$
M_a	Molecular weight of air (kg mol^{-1})
M_W	Molecular weight of water (kg mol^{-1})
m_c	Cold feed stream with time rate of heat capacity (J K^{-1} s^{-1})
m_h	Hot saline feed stream with time rate of heat capacity (J K^{-1} s^{-1})
N''	Permeate flux (kg m^{-2}h^{-1})
$\overline{N''}$	Average permeate flux $S_{N''}$(kg m^{-2}h^{-1})
N_a''	Permeate flux of the air gap (kg m^{-2}h^{-1})
N_m''	Permeate flux in the membrane (kg m^{-2}h^{-1})
N_{exp}	Number of experimental measurements
Nu^R	Enhanced dimensionless Nusselt number
Nu_D	Nusselt number for double-pass modules
Pr	Prandtl number
P_T	System pressure (Pa)
P_m	Mean saturated pressure in membrane (Pa)
P_1^{sat}	Saturated vapor pressure between the hot fluid and membrane surface (Pa)
P_2^{sat}	Saturated vapor pressure between the air gap and membrane surface (Pa)
P_3^{sat}	Saturated vapor pressure between the air gap and condensation surface (Pa)
q_j	Volumetric flow rate (m^3 s^{-1}), $j = h, c$
q_a''	Heat transfer rate between condensation and air gap membrane surface (W m^{-2})
q_f''	Heat transfer rate between condensation and cooling plate (W m^{-2})
q_m''	Heat transfer rate between membrane surface of hot fluid and air gap (W m^{-2})
q_p''	Heat transfer rate of cooling plate (W m^{-2})
q_{cond}''	Heat transfer rate through the membrane (W m^{-2})
q_{ma}''	Heat transfer rate of the membrane to the air gap (W m^{-2})
q_{fc}''	Heat transfer rate of the condensation to the cold fluid (W m^{-2})
q_{vap}''	Heat transfer rate of water evaporation (W m^{-2})
R	Recycle ratio
R_c	Gas constant (8.314 J mol^{-1} K^{-1})
Re	Reynolds number
Re_f	Film Reynolds number

r	Membrane pore radius (m)
$S_{N''}$	Uncertainty of the experimental measurements
$S_{\overline{N''}}$	Mean value of $S_{N''}$
T_1	Temperature of hot fluid membrane surface (°C)
$T_{1,1}$	Temperature of hot fluid membrane surface in the left-hand-side channel (°C)
$T_{1,2}$	Temperature of hot fluid membrane surface in the right-hand-side channel (°C)
T_2	Temperature of air gap membrane surface (°C)
T_3	Temperature of condensation layer surface (°C)
T_4	Temperature of cooling plate surface at permeate side (°C)
T_5	Temperature of cooling plate surface at cold fluid side (°C)
T_c	Temperature of cold fluid (°C)
T_h	Temperature of hot fluid (°C)
$T_{h,1}$	Temperature of hot fluid in the left-hand-side channel (°C)
$T_{h,2}$	Temperature of hot fluid in the right-hand-side channel (°C)
T_m	Mean temperature in membrane (°C)
U_m	The depth-averaged velocity magnitude (m s^{-1})
$\overline{u}$	Average velocity (m s^{-1})
W	Width of channel (m)
x_w	Liquid mole fraction of water
x_{NaCl}	Mole fraction of NaCl in saline solution
Y_w	Vapor mole fraction of water
$\lvert Y_a \rvert_{\ell n}$	Natural log mean vapor mole fraction of water in the air-gap channel
$\lvert Y_m \rvert_{\ell n}$	Natural log mean vapor mole fraction of water in the membrane
z	Axial coordinate along the flow direction (m)
Greek letters	
α^E	Enhancement factor
δ_m	Thickness of membrane (μm)
δ_a	Thickness of air gap (m)
δ_f	Film thickness (m)
δ_p	Thickness of cooling plate (m)
ε	Membrane porosity
η_v	Gas viscosity (Ns m^{-2})
λ	Latent heat of water (J kg^{-1})
λ_{fp}	The mean free path of water vapor in air (m)
μ	Viscosity (Ns m^{-2})
ρ	Density (kg m^{-3})
σ_w	Diffusion volume of water (m^3)
σ_{air}	Diffusion volume of water (m^3)
Γ	The film mass flow per unit width (kg $m^{-1}s^{-1}$)
$\gamma_{m,1}$	Temperature polarization coefficients in the left-hand-side channel
$\gamma_{m,2}$	Temperature polarization coefficients in the right-hand-side channel
τ	Space time (s)
τ_m	Membrane tortuosity
Subscripts	
a	Air gap
c	Cold feed stream
double	Double-pass operations
h	Hot saline feed stream
single	Single-pass operation
exp.	Experimental results
i	At the inlet
e	At the outlet
theo.	Theoretical predictions
Superscripts	
R	Recycling double-pass modules
h	Heat transfer characteristics

Appendix A

Table A1. Validity checks of the model assumptions under the operating conditions of this study.

Check	Value in This Study	Criterion	Conclusion
Linearization of Equation (1) $T_1 - T_3$	≤12.6 K	<15 K [1]	Within validity range
Error of linearized vs. exact Antoine difference	−0.1% to −1.2% (tangent); −0.7% to −2.0% (Clausius–Clapeyron form)	< ±5% (experimental reproducibility)	Negligible, one-signed
Knudsen number $Kn = \lambda_{fp}/d_p$	0.51 ~ 0.55	0.01 < Kn < 1: transition	Knudsen and molecular diffusion both required
Knudsen share of membrane resistance	40 ~ 47%	—	Both mechanisms comparable
Viscous (Poiseuille) flux	0 (no total-pressure difference across pores)	—	Omitted exactly, not approximately
Rayleigh number of air gap Ra_δ (thermal + solutal)	3 ~ 14	$= 10^3$ for onset of convection in tall vertical layers	Pure conduction/diffusion
Condensate film Reynolds number $Re_f = 4\Gamma/\mu$	1.0 ~ 2.7	< 30 (wave-free laminar); < 1800 (laminar)	Nusselt laminar film valid
Maximum condensate film thickness	34 ~ 48 μm (≤ 2.4% of δ_a)	$\ll \delta_a$	No gap bridging
Hydrodynamic entrance length $0.035\,ReD_h$	1.2 ~ 7.9 cm (6 ~ 38% of L)	—	Developing velocity field at high Re
Thermal entrance length$0.05\,RePrD_h$	6 ~ 49 cm	compare with L = 21 cm	Thermally developing; captured by length-averaged regressed Nu
Axial Péclet number Pe = RePr	290 ~ 2460	> 100 [25]	Axial conduction negligible
Richardson number Gr/Re^2 (hot channel)	0.02 ~ 0.17	≥ 0.1: mixed convection	Buoyancy relevant only at the lowest flow rate
Maximum NaCl concentration in module	3.54 wt% (feed 3.50 wt%)	Solubility 26.4 wt%	No NaCl precipitation
Mean residence time of feed in module, $2V/q_h$	8 ~ 24 s, independent of recycle ratio	—	Recycle does not increase mean residence time
Permeate conductivity vs. feed	< 2.0 μS cm^{-1}	—	Apparent salt rejection > 99.99%; no detectable wetting

References

1. Lawson, K.W.; Lloyd, D.R. Membrane distillation. *J. Membr. Sci.* **1997**, *124*, 1–25. [CrossRef]
2. Alkhudhiri, A.; Darwish, N.; Hilal, N. Membrane distillation: A comprehensive review. *Desalination* **2012**, *287*, 2–18. [CrossRef]
3. Ali, A.; Agha Shirazi, M.M.; Nthunya, L.; Castro-Muñoz, R.; Ismail, N.; Tavajohi, N.; Zaragoza, G.; Quist-Jensen, C.A. Progress in module design for membrane distillation. *Desalination* **2024**, *581*, 117584. [CrossRef]
4. Alklaibi, A.M.; Lior, N. Membrane-distillation desalination: Status and potential. *Desalination* **2005**, *171*, 111–131. [CrossRef]

5. Ichiyanagi, M.; Tsutsui, I.; Kakinuma, Y.; Sato, T.; Hishida, K. Three-dimensional measurement of gas dissolution process in gas–liquid microchannel flow. *Int. J. Heat Mass Transf.* **2012**, *55*, 2872–2878. [CrossRef]
6. Klaassen, R.; Feron, P.H.M.; Jansen, A.E. Membrane contactor applications. *Desalination* **2008**, *224*, 81–87. [CrossRef]
7. Olatunji, S.O.; Camacho, L.M. Heat and mass transport in modeling membrane distillation configurations: A review. *Front. Energy Res.* **2018**, *6*, 130. [CrossRef]
8. Yadav, A.; Labhasetwar, P.K.; Shahi, V.K. Membrane distillation using low-grade energy for desalination: A review. *J. Environ. Chem. Eng.* **2021**, *9*, 105818. [CrossRef]
9. Suleman, M.; Asif, M.; Jamal, S.A. Temperature and concentration polarization in membrane distillation: A technical review. *Desalin. Water Treat.* **2021**, *229*, 52–68. [CrossRef]
10. Taamneh, Y.; Bataineh, K. Improving the performance of direct contact membrane distillation utilizing spacer-filled channel. *Desalination* **2017**, *408*, 25–35. [CrossRef]
11. Chang, H.; Hsu, J.-A.; Chang, C.-L.; Ho, C.-D.; Cheng, T.-W. Simulation study of transfer characteristics for spacer-filled membrane distillation desalination modules. *Appl. Energy* **2017**, *185*, 2045–2057. [CrossRef]
12. Tai, Z.S.; Othman, M.H.D.; Koo, K.N.; Jaafar, J. Critical review on membrane designs for enhanced flux performance in membrane distillation. *Desalination* **2023**, *553*, 116484. [CrossRef]
13. Santos, J.; Geraldes, V.; Velizarov, S.; Crespo, J. Investigation of flow patterns and mass transfer in membrane module channels filled with flow-aligned spacers using computational fluid dynamics (CFD). *J. Membr. Sci.* **2007**, *305*, 103–117. [CrossRef]
14. Jeong, S.; Gu, B.; Choi, S.; Ahn, S.; Lee, J.; Jeong, S. Engineered multi-scale roughness of carbon nanofiller- embedded 3D printed spacers for membrane distillation. *Water Res.* **2023**, *231*, 119649. [CrossRef] [PubMed]
15. Shakaib, M.; Hasani, S.M.F.; Mahmood, M. CFD modeling for flow and mass transfer in spacer-obstructed membrane feed channels. *J. Membr. Sci.* **2009**, *326*, 270–284. [CrossRef]
16. Alwatban, A.M.; Mohammed, M.A.; Aljumaily, M.M.; Alsalhy, Q.F. Computational fluid dynamics simulations of desalination processes in vacuum membrane distillation. *Desalin. Water Treat.* **2025**, *322*, 01174. [CrossRef]
17. Welty, J.R.; Wicks, C.E.; Wilson, R.E. *Fundamentals of Momentum, Heat, and Mass Transfer*, 3rd ed.; John Wiley & Sons: New York, NY, USA, 1984.
18. Yeh, H.M.; Tsai, S.W.; Chiang, C.L. Recycle effects on heat and mass transfer through a parallel-plate channel. *AIChE J.* **1987**, *33*, 1743–1746. [CrossRef]
19. Da Costa, A.R.; Fane, A.G.; Wiley, D.E. Spacer characterization and pressure drop modelling in spacer-filled channels for ultrafiltration. *J. Membr. Sci.* **1994**, *87*, 79–98. [CrossRef]
20. Francis, L.; Ahmed, F.E.; Hilal, N. Advances in membrane distillation module configurations. *Membranes* **2022**, *12*, 81. [CrossRef] [PubMed]
21. Marquart, R. Circulation of high-viscosity Newtonian and non-Newtonian liquids in jet loop reactor. *Int. Chem. Eng.* **1981**, *21*, 399–407.
22. Siegel, M.H.; Merchuk, J.C.; Schügerl, K. Air-lift reactor analysis: Interrelationships between riser, downcomer, and gas–liquid separator behavior, including gas recirculation effects. *AIChE J.* **1986**, *32*, 1585–1595. [CrossRef]
23. Jones, A.G. Liquid circulation in a draft-tube bubble column. *Chem. Eng. Sci.* **1985**, *40*, 449–462. [CrossRef]
24. Miyahara, T.; Hamaguchi, M.; Sukeda, Y.; Takahashi, T. Size of bubbles and liquid circulation in a bubble column with a draught tube and sieve plate. *Can. J. Chem. Eng.* **1986**, *64*, 718–725. [CrossRef]
25. Shah, R.K.; London, A.L. *Laminar Flow Forced Convection in Ducts*; Academic Press: New York, NY, USA, 1978.
26. Duong, H.C.; Cooper, P.; Nelemans, B.; Cath, T.Y.; Nghiem, L.D. Optimising thermal efficiency of direct contact membrane distillation by brine recycling for small-scale seawater desalination. *Desalination* **2015**, *374*, 1–9. [CrossRef]
27. Yeh, H.-M. Membrane extraction in rectangular modules with external recycle. *J. Chin. Inst. Chem. Eng.* **2008**, *39*, 679–684. [CrossRef]
28. Liu, J.; Xie, B.; Mushtaq, N.; Xu, G.; Bar-Zeev, E.; Hu, Y. New insights into the role of carbon nanotubes spray-coated on both sides of the PTFE membrane in suppressing temperature polarization and enhancing water flux in direct contact membrane distillation. *J. Membr. Sci.* **2024**, *689*, 122184. [CrossRef]
29. Ho, C.-D.; Li, C.-Y.; Chew, T.L.; Lin, Y.-T. Theoretical and experimental studies of permeate fluxes in double-flow direct-contact membrane distillation (DCMD) modules with internal recycle. *Membranes* **2026**, *16*, 37. [CrossRef] [PubMed]
30. Fukazawa, T.; Kawamura, H.; Tamura, T. Water vapour resistance of hydrophobic microporous membranes under reduced pressure at a constant temperature. *J. Text. Inst.* **1999**, *4*, 602–615. [CrossRef]
31. Xiong, L.P.; Yu, W.; Ji, C.L.; Liu, L.Y.F.; Teng, J.H.; Chen, C.; Lin, H.J.; Shen, L.G. Bio-derived carboxymethyl cellulose-graft-gallic acid antiscalant with remarkable antibacterial activity for reverse osmosis scaling and biofouling control. *Water Res.* **2025**, *281*, 123716. [CrossRef] [PubMed]

32. Xie, M.J.; Yang, W.F.; Zhou, X.N.; Wang, B.Y.; Liu, J.Q.; Xu, X.; Shen, L.G.; Zhang, H.M.; Zhang, M.J.; Yu, W.; et al. Multiscale thermodynamic insights into membrane fouling control by biochar-activated peroxymonosulfate pretreatment: Synergy of oxidation and adsorption. *Water Res. Part A* **2026**, *288*, 124564. [CrossRef] [PubMed]
33. Yao, X.Y.; Li, R.J.; Shen, L.G.; Zhao, L.H.; Lin, H.J. A novel magnetically induced Co@NC-modified electrochemical membrane for continuous peroxymonosulfate activation: Achieving ultrafast and cost-effective purification with elucidation of mechanism and application potential. *Water Res. Part B* **2025**, *287*, 124436. [CrossRef] [PubMed]
34. Sun, J.H.; Yan, M.J.; Tao, G.D.; Su, R.B.; Xiao, X.M.; Wu, Q.S.; Chen, F.; Wu, X.L.; Lin, H.J. A single-atom manganese nanozyme mediated membrane reactor for water decontamination. *Water Res. Part A* **2025**, *268*, 122627. [CrossRef] [PubMed]
35. Zhang, J.H.; Gary, H.; Li, J.D. Modeling heat and mass transfers in DCMD using compressible membranes. I. Knudsen-Poiseuille transition. *J. Membr. Sci.* **2012**, *387–388*, 7–16.
36. Schofield, R.W.; Fane, A.G.; Fell, C.J.D. Gas and vapor transport through microporous membranes. I. Knudsen-Poiseuille transition. *J. Membr. Sci.* **1990**, *53*, 159–171. [CrossRef]
37. Lawson, K.W.; Lloyd, D.R. Membrane distillation. II. Direct contact MD. *J. Membr. Sci.* **1996**, *120*, 123–133. [CrossRef]
38. Iversen, S.B.; Bhatia, V.K.; Dam-Jphasen, K.K.; Jonsson, G. Characterization of microporous membranes for use in membrane contactors. *J. Membr. Sci.* **1997**, *130*, 205–217. [CrossRef]
39. Alklaibi, A.M.; Lior, N. Transport analysis of air-gap membrane distillation. *J. Membr. Sci.* **2005**, *255*, 239–253. [CrossRef]
40. Banat, F.A.; Simandl, J. Membrane distillation for dilute ethanol: Separation from aqueous streams. *J. Membr. Sci.* **1999**, *163*, 333–348.
41. Incropera, F.P.; DeWitt, D.P.; Bergman, T.L.; Lavine, A.S. *Fundamentals of Heat and Mass Transfer*, 6th ed.; John Wiley & Sons: Hoboken, NJ, USA, 2007.
42. Bouguecha, S.; Chouikh, R.; Dhahbi, M. Numerical study of the coupled heat and mass transfer in membrane distillation. *Desalination* **2003**, *152*, 245–252. [CrossRef]
43. ElSherbiny, S.M.; Raithby, G.D.; Hollands, K.G.T. Heat transfer by natural convection across vertical and inclined air layers. *J. Heat Transf.* **1982**, *104*, 96–102. [CrossRef]
44. Warner, S.B. *Fiber Science*; Princeton-Hall: Englewood Cliffs, NJ, USA, 1995.
45. Bird, R.B.; Stewart, W.E.; Lightfoot, E.N. *Transport Phenomena*; John Wiley & Sons, Inc.: New York, NY, USA, 2002.
46. Taylor, G.I. Dispersion of soluble matter in solvent flowing slowly through a tube. *Proc. R. Soc. A* **1953**, *219*, 186–203. [CrossRef]
47. Phattaranawik, J.; Jiraratananon, R.; Fane, G.A. Effect of pore size distribution and air flux on mass transport in direct contact membrane distillation. *J. Membr. Sci.* **2003**, *215*, 75–85. [CrossRef]
48. Phattaranawik, J.; Jiraratananon, R.; Fane, A.G. Heat transport and membrane distillation coefficients in direct contact membrane distillation. *J. Membr. Sci.* **2003**, *212*, 177–193. [CrossRef]
49. Sarkar, J. A critical review on convective heat transfer correlations of nanofluids. *Renew. Sustain Energy Rev.* **2011**, *15*, 3271–3277. [CrossRef]
50. Kern, D.Q. *Process Heat Transfer*; McGraw-Hill: New York, NY, USA, 1950.
51. Kandlikar, S.G.; Schmit, D.; Carrano, A.L.; Taylor, J.B. Characterization of surface roughness effects on pressure drop in single-phase flow in mini channels. *Phys. Fluids* **2005**, *17*, 100606. [CrossRef]
52. Kakac, S.; Shah, R.K.; Aung, W. *Handbook of Single-Phase Convective Heat Transfer*; Wiley: New York, NY, USA, 1987.
53. Menter, F.R. Two-equation eddy-viscosity turbulence models for engineering applications. *AIAA J.* **1994**, *32*, 1598–1605. [CrossRef] [PubMed]
54. Levenspiel, O. *Chemical Reaction Engineering*, 3rd ed.; John Wiley & Sons: New York, NY, USA, 1999.
55. Moffat, R.J. Describing the uncertainties in experimental results. *Exp. Therm. Fluid Sci.* **1988**, *1*, 3–17. [CrossRef]
56. Ho, C.D.; Chen, L.; Yang, Y.L.; Chen, S.T.; Lim, J.W.; Chen, Z.Z. Permeate Flux Enhancement in Air Gap Membrane Distillation Modules with Inserting Λ-ribs Carbon-Fiber Open Slots. *Membranes* **2023**, *13*, 66–85. [CrossRef] [PubMed]

Disclaimer/Publisher's Note: The statements, opinions and data contained in all publications are solely those of the individual author(s) and contributor(s) and not of MDPI and/or the editor(s). MDPI and/or the editor(s) disclaim responsibility for any injury to people or property resulting from any ideas, methods, instructions or products referred to in the content.